Marine and Petroleum Geology 121 (2020) 104622

Contents lists available at ScienceDirect

Marine and Petroleum Geology

journal homepage: www.elsevier.com/locate/marpetgeo

Research paper

# Distinct evolution trends of nanometer-scale pores displayed by the pyrolysis of organic matter-rich lacustrine shales: Implications for the pore development mechanisms

Huijuan Guo [a,b], Wanglu Jia [a,*], Ruliang He [a,b], Chiling Yu [a], Jianzhong Song [a], Ping'an Peng [a,b]

[a] State Key Laboratory of Organic Geochemistry, Guangzhou Institute of Geochemistry, Chinese Academy of Sciences, Guangzhou, 510640, China
[b] University of Chinese Academy of Sciences, Beijing, 100049, China

ARTICLE INFO

*Keywords:*
Organic matter type
Total organic carbon
Nanometer-scale pore
Pyrolysis simulation
Hydrocarbon expulsion

ABSTRACT

Organic matter (OM) compositions greatly affect hydrocarbon generation and expulsion processes, which are critical for the organic porosity development in shale. Lacustrine shale samples of low thermal maturity were pyrolyzed using two pyrolysis systems (closed and semi-closed systems). Pore development was measured by low-pressure gas adsorption and field emission-scanning electron microscopy (FE-SEM), and bulk porosity was modeled utilizing organic geochemical data. The gas adsorption analysis indicated that shale samples of different OM compositions differed in pore volume evolution with thermal maturity, mainly related to the different amounts of hydrocarbon generated and expelled. Residual bitumen significantly reduced the pore volume of OM-rich oil generative shale samples, and restricted the micro-, meso-, and macro-pore volumes to different extents. Calculations and experiments both showed that OM-rich and oil generative shale experienced a greater increase in pore volume after the oil peak. In addition, it was observed that variations in the main pore types were associated both with shale compositions and with exerted overburden pressure. Increase in overburden pressure were found to greatly facilitate the development of nanometer-size spongy and complex OM pores in shales containing type II/III kerogens, possibly as a result of the expulsion of gaseous hydrocarbons. By contrast, the shale with abundant type I kerogen tended mainly to develop relatively large pores following oil expulsion regardless of overburden pressure. The modeled organic porosity of pyrolyzed samples of type III OM was similar to the porosity of geological shale, but the porosity of OM-rich oil generative shale samples with high expulsion efficiency at the oil generation stage was two to three times the measured porosity of the geological shale. In some cases, the higher modeled shale porosity might be related to the higher expulsion efficiency. For geological shales of expulsion efficiency comparable to the pyrolyzed samples, geological processes (e.g., compaction and cementation) may have greatly reduced the OM-associated pore volume.

## 1. Introduction

The porosity and pore structure of shale are critical, both for the evaluation of shale gas/oil storage capacity and for primary migration of hydrocarbons (Bustin et al., 2008; Eseme et al., 2012). Shale reservoirs are basically different from conventional reservoirs due to their relatively high content of indigenous organic matter (OM), thermally evolved products of kerogen. Successive transformation processes of kerogen as well as its degradation products lead to significant changes in the mass and volume of various kinds of shale OM during thermal maturation, which has been thought to be a key reason for organic pore development in shales (Jarvie et al., 2007; Loucks et al., 2009) and thus forms the theoretical basis for predicting porosity during the maturation of shale (Chen and Jiang, 2016; Eseme et al., 2012; Han et al., 2017; Modica and Lapierre, 2012). Nevertheless, the mechanisms and quantification of pore development with relation to the transformations of OM are complex and have not been deeply explored to date: see the latest review by Katz and Arango (2018) and references therein. Pore characterizations on geological samples by many techniques have provided unambiguous evidence for either increase or decrease of shale porosity through the transformation and/or migration of different kinds of OM e.g., hydrocarbon generation and resulting mass loss of kerogen (Chukwuma et al., 2018; Liu et al., 2017a; Loucks et al., 2009; Löhr et al., 2015), the expansion and shrinkage of kerogen due to the

* Corresponding author.
*E-mail address:* wljia@gig.ac.cn (W. Jia).

https://doi.org/10.1016/j.marpetgeo.2020.104622
Received 13 April 2020; Received in revised form 13 July 2020; Accepted 27 July 2020
Available online 1 August 2020

retention and expulsion of its produced oil (Alcantar-Lopez, 2016; Mathia et al., 2016), the infilling of mineral-related pores by migrated oil (Guo et al., 2018; Löhr et al., 2015; Pommer and Milliken, 2015), the formation of pyrobitumen by residual oil cracking and hydrocarbon expulsion or exsolution (Bernard et al., 2012; Cardott et al., 2015; Loucks and Reed, 2014; Tian et al., 2015). The original OM compositions in the shale greatly influence the extent of these processes, in addition to other factors, which may include mineral matrix, pressure and rock texture (Guo et al., 2017; Ji et al., 2017; Kelemen et al., 2006; Mathia et al., 2016; Pepper and Corvi, 1995; Pommer and Milliken, 2015). Thus, it seems that OM compositions probably affect porosity evolution in shale during thermal maturation.

Positive correlations between total organic carbon (TOC) content and bulk porosity and specific pore volume have been widely reported for shales at various maturity levels, mostly after the oil peak (with equivalent vitrinite reflectance of 1.1–4.3%) (Chukwuma et al., 2018; Milliken et al., 2013; Tian et al., 2015; Zeng et al., 2016); however, this trend does not usually persist into the relatively high TOC content ranges (Chukwuma et al., 2018; Milliken et al., 2013; Pan et al., 2015; Zeng et al., 2016). In the case of shale within the oil window, weak relationships if any were commonly observed (Furmann et al., 2014; Guo et al., 2018; Ko et al., 2017; Liu et al., 2017a,b,c; Loucks et al., 2017). A notable decrease in OM porosity and the size both of pores and pore throats with increasing TOC have been demonstrated, possibly the consequence of high gas expulsion and consequent pore collapse, as evidenced by both greater OM connectivity and easier framework compaction in high-TOC shales (Dong et al., 2017; Mathia et al., 2016; Milliken et al., 2013; Ross and Bustin, 2009). Moreover, OM type has a crucial effect on OM-hosted pores (Ardakani et al., 2017; Curtis et al., 2011; Guo et al., 2018; Liu et al., 2017a; Löhr et al., 2015; Milliken et al., 2013). Types II/III and III kerogens have higher micropore volumes than types I and II, based on per unit TOC values (Chalmers and Bustin, 2008). Terrigenous type III kerogen is usually non-porous (Guo et al., 2018; Klaver et al., 2015; Löhr et al., 2015; Loucks et al., 2012, 2017; Pommer and Milliken, 2015) or may be porous under field emission scanning electron microscopy (FE-SEM) observation (Fishman et al., 2012; Lu et al., 2015). The differences may be related to the preservation of original structure (Guo et al., 2018; Loucks et al., 2017). Different kinds of macerals in shale show different pore evolution trends during thermal maturation (Cardott and Curtis, 2018; Klaver et al., 2015; Ko et al., 2018; Liu et al., 2017a; Löhr et al., 2015). The size, shape and occurrence of the OM are also important aspects, and probably reflect compaction effect (e.g., pores are much less developed in laminar OM than in OM dispersed between mineral grains) (Guo et al., 2018; Löhr et al., 2015).

Besides studies on geological samples, thermal simulation has been an important complementary approach to understanding pore development mechanisms in shale. Pyrolysis in a vacuum closed-system study of two mudstones with relatively high TOC content indicated that the pore volume and specific surface area increased greatly with increasing thermal maturity, but decreased in one organic-lean mudstone (Chen and Xiao, 2014). This clearly demonstrated the important transformation role of OM on pore development in shale. Subsequently, many studies have examined various thermal simulation systems at different pressures and openness conditions, both dry (anhydrous) or in the presence of water (hydrous), to elucidate the effects of evolution and expulsion of OM on shale pore development (Cavelan et al., 2019; Cui et al., 2013; Guo et al., 2017; Hu et al., 2015; Ji et al., 2017; Ko et al., 2016, 2018; Liu et al., 2017b, 2019; Sun et al., 2015; Wang et al., 2019; Wu et al., 2015). Hydrous pyrolysis of shales has revealed that mesopores within OM contribute greatly to shale pore development, and that the development of 2–6 nm pores controls the methane-adsorption capacity of shale (Hu et al., 2015; Sun et al., 2015). Anhydrous pyrolysis combined with SEM has revealed different degrees of development for pores related to OM and minerals at different maturity stages (Ji et al., 2017; Ko et al., 2016, 2018), such as mineral-modified pores and spongy pores within the OM. Low-pressure gas ($N_2$, $CO_2$) adsorption analysis of pyrolyzed samples under high-pressure anhydrous conditions has shown that oil expulsion greatly influences the pore development in lacustrine types I and II shales (Guo et al., 2017; Liu et al., 2017b). However, these studies generally focused on only one type of shale, and thus the impact of OM compositions were not discussed.

Two recent studies have provided some insight into this topic. Based on their previous pyrolysis studies on the Eagle Ford shale, Ko et al. (2018) have used FE-SEM to investigate the pore development of three Barnett and Woodford shale samples with different OM compositions, under high fluid pressure and anhydrous conditions, combined with variations in OM content (gas, oil and its fractions, and residual kerogen). This study demonstrates that differences in the chemical composition and hydrocarbon generation kinetics between different macerals, which also vary in individual shale samples, are responsible for the differences in pore evolution trends (Ko et al., 2018). Cavelan et al. (2019) conducted thermal maturation of marine shale samples from the same formation and showed that variations in the individual particulate OM assemblage of a similar type II kerogen significantly influence the amount of oil and gas generated during thermal maturation, resulting in different pore evolution models. Gas adsorption analysis has shown that hydrostatic and lithostatic pressures play insignificant roles in pore volume evolution in pyrolyzed samples with distinctive OM compositions at relatively low maturity levels (Mastalerz et al., 2018).

In the present study, two lacustrine samples (one with highly abundant type I OM and the other with about 5 wt% of type III OM) were pyrolyzed and analyzed for changes in organic geochemistry and pore volume using the same technique as reported by Guo et al. (2017) for a lacustrine sample with highly abundant type II OM. The impacts of OM compositions on pore evolution trends and pore development mechanisms were thus qualitatively explored by combining results from the three lacustrine shale samples. In addition, this data was input into different predication models for the development of both organic and kerogen porosities with increasing maturity, based on variations in the residual TOC content or the amount of expelled OM (Chen and Jiang, 2016; Peters et al., 2005). Calculated results were tentatively used to quantify the development degree of organic porosity for shales with different OM compositions during progressive thermal maturation.

## 2. Sample preparation and experiment method

### 2.1. Samples

Our previous study (Guo et al., 2017) used a sample of shale Y2 from the Chang 7 Member, Ordos Basin, with high TOC content (18.7 wt%) and a moderate hydrogen index (HI) of 428 mg HC/g TOC representing type II kerogen for pyrolysis. This sample was collected from the outcrop located at the Tangnihe village of Tongchuan (Fig. 1). The Ordos Basin, with immense proved reserves, is one of the most productive petroliferous basins in China (Yang et al., 2013). OM-rich shales are mainly distributed in the Chang 7 Member of the lacustrine Yanchang Formation. The shale has been demonstrated to be one of the most promising hybrid shale oil/shale gas systems in lacustrine strata in China (Lei et al., 2015; Wang et al., 2014; Yang et al., 2013). For comparison, another sample (no. Y11) from this member, with a moderate TOC content (5.28 wt%) and relatively low HI (214 mg/g TOC) was used to represent samples having type III kerogen (Table 1). Y11 was a core sample collected from a well located at Xiasiwan oil field (Fig. 1). Another lacustrine shale sample (no. MM15) containing type I kerogen was collected for comparison, since type I kerogen has seldom been reported for the Chang 7 Member. This sample is from the Paleogene Youganwo Formation in the Maoming Basin, South China (Fig. 1). The formation is well known for production of oil shale in China; average oil content is mainly between 5.71 wt% and 8.39 wt%, with the largest content about 11.9 wt% (Guo et al., 2009). The sample used in this study had a high

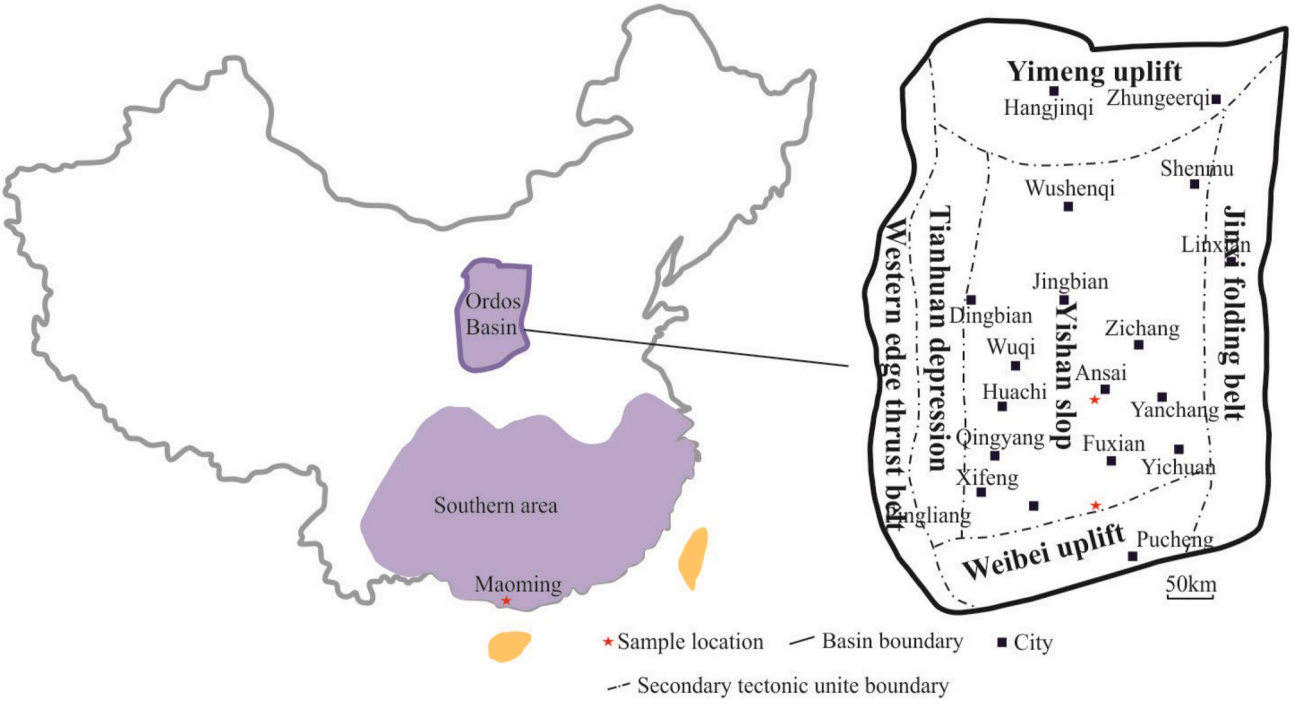


**Fig. 1.** Simplified maps of China and Ordos Basin showing the sample locations (modified after Zou et al., 2019).

**Table 1**
Geochemical parameters and pore volume of pyrolyzed samples MM15 and Y11.

| Sample | S1 | S2 | Tmax | TOC | HI | OI | Volume ($cm^3$/100 g) | | | | Average pore width |
|---|---|---|---|---|---|---|---|---|---|---|---|
| | (mg/g) | (mg/g) | (°C) | (wt%) | (mg/g TOC) | (mg/g TOC) | Micropore | Mesopore | Macropore | Total | (nm) |
| MM15-O | 1.63 | 122.25 | 435 | 17.52 | 698 | 14 | 0.25 (0.41) | 4.99 (4.48) | 4.42 (2.67) | 9.71 (7.61) | 20.95 (16.82) |
| Y11–O | 3.61 | 11.29 | 438 | 5.28 | 214 | 11 | 0.14 | 1.07 | 0.74 | 1.95 | 15.11 |
| MM15-C-330 | 11.55 | 73.78 | 443 | 13.62 | 542 | 3 | 0.10 | 1.08 | 3.29 | 4.50 | 30.97 |
| MM15-C-350 | 19.8 | 45.62 | 442 | 12.6 | 362 | 2 | 0.12 | 2.21 | 4.59 | 6.97 | 31.14 |
| MM15-C-380 | 13.57 | 22.36 | 515 | 11.06 | 202 | 1 | 0.19 | 3.76 | 6.21 | 10.22 | 29.28 |
| MM15-C-420 | 3.66 | 2.45 | 585 | 9.65 | 25 | 3 | 0.31 | 3.87 | 6.04 | 10.30 | 26.46 |
| MM15-C-450 | 3.21 | 1.36 | 607 | 9.94 | 14 | 2 | 0.34 | 4.13 | 6.53 | 11.08 | 26.82 |
| MM15-C-500 | 2.72 | 0.74 | – | 11.11 | 7 | 2 | 0.35 | 4.32 | 5.75 | 10.50 | 24.46 |
| MM15-C-560 | 2.64 | 0.56 | – | 11.11 | 5 | 4 | 0.33 | 4.82 | 6.68 | 11.90 | 25.83 |
| MM15-SC-330 | 7.62 | 114.7 | 441 | 15.87 | 723 | 4 | 0.10 | 0.35 | 0.76 | 1.22 | 35.53 |
| MM15-SC-350 | 5.27 | 88.3 | 441 | 12.93 | 683 | 5 | 0.11 | 0.36 | 0.71 | 1.18 | 39.26 |
| MM15-SC-380 | 5.69 | 72.8 | 441 | 11.53 | 631 | 4 | 0.14 | 0.73 | 1.06 | 1.94 | 35.24 |
| MM15-SC-420 | 0.93 | 14.25 | 442 | 6.57 | 217 | 5 | 0.24 | 3.15 | 2.25 | 5.67 | 23.90 |
| MM15-SC-450 | 0.72 | 4.32 | 450 | 5.56 | 78 | 4 | 0.25 | 3.58 | 2.93 | 6.80 | 20.31 |
| MM15-SC-500 | 0.06 | 0.71 | 597 | 5.83 | 12 | 1 | 0.38 | 5.32 | 4.21 | 9.95 | 22.84 |
| MM15-SC-560 | 0.01 | 0.07 | 609 | 4.41 | 2 | 10 | 0.39 | 5.39 | 4.23 | 10.04 | 22.76 |
| Y11–C-330 | 2.9 | 7.67 | 447 | 4.65 | 165 | 7 | 0.10 | 0.84 | 0.76 | 1.70 | 21.17 |
| Y11–C-350 | 2.33 | 4.27 | 458 | 4.65 | 92 | 8 | 0.13 | 1.08 | 0.95 | 2.16 | 20.77 |
| Y11–C-380 | 1.34 | 1.45 | 559 | 4.39 | 33 | 7 | 0.17 | 1.22 | 1.05 | 2.44 | 20.51 |
| Y11–C-420 | 0.68 | 0.89 | 590 | 4.47 | 20 | 5 | 0.17 | 1.15 | 1.03 | 2.35 | 21.08 |
| Y11–C-450 | 1.61 | 0.39 | 609 | 4.19 | 9 | 6 | 0.21 | 1.40 | 1.29 | 2.90 | 20.02 |
| Y11–C-500 | 1.23 | 0.23 | – | 4.13 | 6 | 14 | 0.26 | 1.62 | 1.43 | 3.31 | 18.94 |
| Y11–C-540 | 1.01 | 0.23 | – | 4.33 | 5 | 15 | 0.26 | 1.68 | 1.58 | 3.52 | 19.57 |
| Y11-SC-330 | 0.78 | 8.98 | 445 | 4.39 | 205 | 2 | 0.10 | 1.17 | 0.85 | 2.12 | 17.41 |
| Y11-SC-350 | 1.45 | 8.81 | 444 | 4.41 | 200 | 7 | 0.10 | 0.96 | 0.78 | 1.84 | 18.91 |
| Y11-SC-380 | 1.13 | 7.92 | 446 | 4.4 | 180 | 6 | 0.10 | 1.01 | 0.87 | 1.98 | 19.44 |
| Y11-SC-420 | 1.07 | 4.65 | 453 | 4.23 | 110 | 8 | 0.14 | 1.04 | 0.94 | 2.12 | 20.24 |
| Y11-SC-450 | 1.06 | 2.79 | 461 | 4.22 | 66 | 7 | 0.16 | 1.13 | 1.00 | 2.29 | 20.37 |
| Y11-SC-500 | 0.03 | 0.5 | 596 | 3.79 | 13 | 4 | 0.30 | 1.97 | 1.32 | 3.59 | 14.95 |
| Y11-SC-540 | 0.04 | 0.08 | 609 | 4.01 | 2 | 9 | 0.38 | 2.15 | 1.46 | 3.98 | 15.51 |

MM15-O, Y11–O represents the original MM15 and Y11 samples; the others are named in the "MM15 (Y11)-pyrolysis system-pyrolysis temperature" style. C and SC represent the closed and semi-closed system, respectively, e.g., MM15-C-330 represents the sample pyrolyzed at 330 °C in the closed system. For sample MM15-O, values in brackets indicate pore volume of the sample after compaction at 80 MPa.

TOC content of 17.52 wt% and a high HI (698 mg/g TOC), representing shale with abundant type I kerogen. Both sample Y11 and MM15 were marginally mature, as indicated by their relatively low Tmax values (438 and 435 °C).

### 2.2. Pyrolysis experiment

The experimental scheme has been detailed in a previous study (Guo et al., 2017). Briefly, the samples were first polished to remove the oxidized surface and cleaned with deionized water, then crushed to 0.83–4 mm size and homogeneously mixed. Two distinct pyrolysis systems were used for artificially thermal maturation: one was the glass tube sealed under vacuum conditions (closed system); the other was a semi-closed pressured system. For the closed system, 0.6–3 g samples were introduced into the glass tube, as the large amount of gas generated at high temperatures created a pressure high enough to break the glass tube of which the pressure tolerance is about 600 kPa. Pressure in the glass tube during thermal simulation was estimated to be smaller than 300 kPa. For the semi-closed system, 25–30 g particles were put into a stainless-steel cylinder with inner diameter 34 mm, and an overburden pressure of 80 MPa was then applied to the sample particles from the top down to compact them. Expelled oils flowed out of the system through a slim tube at the base of the apparatus upon elevated temperatures and exerted internal fluid pressure. The pyrolysis in both systems was performed similarly, by isothermal heating of the samples for 48 h at 330, 350, 380, 420, 450, 500, 540 and 560 °C.

### 2.3. Organic geochemistry

Samples of about 50 mg were analyzed by a Vinci Technologies' Rock-Eval 6 instrument to characterize the composition and content of residual OM in the pyrolyzed samples. Information about residual hydrocarbon content and potential was obtained from the analysis.

### 2.4. Mineralogy

X-ray diffraction (XRD) was used to identify minerals and other crystalline phases of the raw and pyrolyzed shale samples and the content of individual clay mineral in clay fractions separated from the shale rock powder. For the analysis of individual clay mineral content in clay fractions, at least 20 g shale power was needed. However, for the pyrolyzed samples, the amount of shale samples for each pyrolysis temperature was not enough for the analysis. Therefore, only the mineral composition of the whole rock sample was analyzed for the pyrolyzed samples. As it is difficult to distinguish between illite/smectite mixed-layer mineral (I/S) and illite during the analysis of mineral composition for the whole-shale samples, I/S was identified as illite. The mineral composition was determined using a Rigaku D/Max-RB diffractometer (Cu Kα radiation ($\lambda = 0.15418$ nm), 40 kV, 100 mA) and a scan rate of 4° (2θ/)/min was used in the range 5–45° to record XRD traces for clay fractions and in the range 3–70° to record XRD traces of minerals in raw shale samples. The experiment and measurement were conducted according to the oil and gas industry standards of the People's Republic of China named "Analysis method for clay minerals and ordinary non-clay minerals in sedimentary rocks by the X-ray diffraction" (China Petroleum Standardization Committee, 2010).

### 2.5. Low-pressure $CO_2$ and $N_2$ gas adsorption

The surface area, pore volume and pore size distribution of the samples were determined by low pressure $CO_2$ and $N_2$ adsorption using a Micromeritics ASAP 2460 analyzer on samples crushed to 80 mesh and dried in a vacuum oven for 24 h at 110 °C. Before adsorption, the samples were degassed by the Micromeritics instrument for 12–24 h to remove adsorbed gas and moisture.

Low-pressure $CO_2$ adsorption was used to measure the volume and surface area of micropores (<2 nm), and the adsorption of gas in micropore is volume filling (Sing, 1985). The relative pressure ($P/P_0$, where P is the gas vapor pressure and $P_0$ is the saturated gas vapor pressure at the given temperature) was between $3 \times 10^{-5}$ and $3 \times 10^{-2}$ at a constant temperature of 0 °C. The surface area and volume were determined using the density functional theory model included in the software of Micromeritics instrument.

Low-pressure $N_2$ adsorption was performed using a temperature of −196 °C and relative pressures of 0.005–0.995. The pore volume and pore size distribution for 1.7–300 nm were determined by the Barrett, Joyner and Halenda (BJH) model using the adsorption branch, because the desorption branch is much more affected by the pore network (Barrett et al., 1951; Groen et al., 2003).

### 2.6. Field emission-scanning electron microscopy (FE-SEM)

A flat surface was prepared from a portion of rock particles for FE-SEM analysis by an Ar ion-beam milling instrument (Hitachi IM4000). Each sample was milled at acceleration voltages of 6 kv for 1.5 h and 4 kv for 0.5 h. A Hitachi S8010 SEM system equipped with secondary electron (SE) and backscattered electron (BSE) detectors was used to image pores and their association with OM and mineral grains under an accelerating voltage of 1.5 kv and a working distance of 3–8 mm. The detection limit was 5 nm at a working distance of 3 mm. JMicroVision software was used to measure the size of pores. As the pore shapes are mostly irregular, pore diameter is the equivalent circular diameter.

## 3. Results

### 3.1. Mineral composition

Shale sample no. Y11 was dominated by clay (33%), quartz (30%) and feldspar (30%), with minor minerals including pyrite (3%) and siderite (4%) (Table 2). In shale sample no. MM15, quartz (28%) and clay mineral (56%) were the main minerals together with 12% feldspars and 4% pyrite. In shale sample no. Y2 also collected at the outcrop, the main mineral composition was clay (25%), quartz (24%), feldspars (16%) and melanterite (20%). Clay minerals included mixed-layer illite/smectite, kaolinite, illite and chlorite in various concentrations. The I/S was generally the dominant clay mineral in the three raw shale samples.

As stated above, the illite content in pyrolyzed shale samples included some I/S (Table 2). Generally, the illite content increased with increasing thermal simulation temperature, except for the closed system of MM15 and Y11 (Table 2). For pyrolyzed samples of Y2, quartz content increased with thermal simulation temperature. However, for the other two samples, Y11 and MM15, the quartz content showed little variation (Table 2). Relatively high content of melanterite might be a result of slight weathering.

### 3.2. Variation of OM during pyrolysis

Pyrolysis condition-dependent evolution trends of OM for samples Y11 and MM15 (Fig. 2) agree well with those previously reported for sample Y2 with abundant type II kerogen (Guo et al., 2017). For Y2 in that report, the maturation of OM, especially the secondary cracking of residual bitumen, occurs much more slowly in a semi-closed than in a closed system. Greater carbon loss (up to 6 wt%) was shown by pyrolyzed samples in the semi-closed system relative to those in the closed system (<3 wt%). This demonstrates that the OM transformation and hydrocarbon expulsion processes are distinctly different with respect to sample composition and pyrolysis system.

From the original condition to 560 °C, the TOC content of pyrolyzed samples of MM15 displayed decreases of about 13 wt% (semi-closed system) and 6.5 wt% (closed system) (Fig. 2a, Table 1). By contrast, the decreases (~1.3 wt% and ~1 wt%, respectively) were much less for pyrolyzed Y11 samples (Fig. 2e). Tmax values agree well at pyrolysis temperatures of 330 °C and 350 °C (Fig. 2b, f), but a sharp increase is seen in Tmax at 380 °C in the closed system, followed by a small increase at pyrolysis temperatures above 420 °C. By contrast, Tmax values in the semi-closed system were almost unchanged over this temperature interval, then increased sharply between 450 °C and 500 °C and after that

**Table 2**
Mineralogical composition of original and artificially matured shale samples.

| Sample | Quartz | Feldspar | Pyrite | Gypsum | Melanterite | Jarosit | Siderite | Kaolinite | Chlorite | Illite | I/S | Mixed layer ratio(%S) |
|---|---|---|---|---|---|---|---|---|---|---|---|---|
| | % | % | % | % | % | % | % | % | % | % | % | I/S |
| MM15 | 28 | 12 | 4 | – | – | – | – | 24 | – | 4 | 28 | 40 |
| Y2 | 24 | 16 | 7 | 9 | 20 | – | – | – | – | 4 | 22 | 15 |
| Y11 | 30 | 30 | 3 | – | – | – | 4 | 2 | 2 | 3 | 26 | 10 |
| MM15-BL-330 | 37 | 15 | – | – | – | – | – | 19 | – | 29 | – | – |
| MM15-BL-350 | 40 | 14 | – | – | – | – | – | 15 | – | 31 | – | – |
| MM15-BL-380 | 37 | 15 | – | – | – | – | – | 15 | – | 32 | – | – |
| MM15-BL-420 | 37 | 16 | – | – | – | – | – | 17 | – | 30 | – | – |
| MM15-BL-450 | 39 | 17 | – | – | – | – | – | 22 | – | 21 | – | – |
| MM15-BL-500 | 40 | 20 | – | – | – | – | – | 22 | – | 18 | – | – |
| MM15-YJ-330 | 37 | 16 | 4 | – | – | – | – | 24 | – | 19 | – | – |
| MM15-YJ-350 | 36 | 16 | 4 | – | – | – | – | 23 | – | 21 | – | – |
| MM15-YJ-380 | 38 | 17 | 4 | – | – | – | – | 21 | – | 20 | – | – |
| MM15-YJ-420 | 36 | 16 | 3 | – | – | – | – | 15 | – | 30 | – | – |
| MM15-YJ-450 | 37 | 17 | – | – | – | – | – | 16 | – | 31 | – | – |
| Y2-BL-330 | 24 | 17 | 5 | – | 28 | – | – | – | – | 25 | – | – |
| Y2-BL-350 | 21 | 19 | 4 | – | 32 | – | – | – | – | 23 | – | – |
| Y2-BL-380 | 28 | 16 | 6 | – | 9 | 11 | – | – | – | 30 | – | – |
| Y2-BL-450 | 35 | 20 | – | – | – | 6 | – | – | – | 32 | – | – |
| Y2-BL-500 | 35 | 20 | – | – | – | 6 | – | – | – | 29 | – | – |
| Y2-YJ-330 | 19 | 17 | 4 | – | 29 | 6 | – | – | – | 25 | – | – |
| Y2-YJ-350 | 16 | 19 | 4 | – | 34 | 5 | – | – | – | 23 | – | – |
| Y2-YJ-380 | 16 | 16 | 5 | – | 32 | 6 | – | – | – | 24 | – | – |
| Y2-YJ-420 | 19 | 17 | 6 | – | 26 | 7 | – | – | – | 25 | – | – |
| Y2-YJ-450 | 31 | 18 | 4 | – | 5 | 13 | – | – | – | 29 | – | – |
| Y2-YJ-500 | 34 | 20 | – | – | – | 8 | – | – | – | 38 | – | – |
| Y11-BL-330 | 30 | 29 | – | – | – | – | – | 9 | – | 31 | – | – |
| Y11-BL-350 | 28 | 30 | – | – | – | – | – | 8 | – | 34 | – | – |
| Y11-BL-380 | 33 | 31 | – | – | – | – | – | 11 | – | 25 | – | – |
| Y11-BL-450 | 29 | 32 | – | – | – | – | – | 9 | – | 31 | – | – |
| Y11-BL-500 | 33 | 30 | – | – | – | – | – | 8 | – | 28 | – | – |
| Y11-YJ-330 | 32 | 35 | – | – | – | – | – | 10 | – | 23 | – | – |
| Y11-YJ-500 | 33 | 32 | – | – | – | – | – | 10 | – | 26 | – | – |
| Y11-YJ-560 | 31 | 33 | – | – | – | – | – | – | – | 37 | – | – |

I/S = illite-smectite mixed layer mineral.

it changed little.

In the closed system, HI values for samples generally showed a gradual decrease with increasing pyrolysis temperature, almost to zero at above 420 °C (Fig. 2c, g). In the semi-closed system, the HI values showed very little variation with temperature up to 380 °C, then a gradual decrease with increasing temperature, approaching zero above 450–500 °C. For the relative amount of residual free hydrocarbons (TOC-normalized ratio S1/TOC, Fig. 2d, h), sample MM15 in the closed system increased rapidly with rising pyrolysis temperature up to 350 °C (Fig. 2d), then a rapid decrease, thus forming a normal oil peak shape. However, in the semi-closed system this ratio showed a smaller increase at 330 °C, then remained almost constant up to 380 °C followed by a decrease with further heating. For sample Y11, which contained type III OM (Fig. 2h), the S1/TOC ratio in the closed system generally decreased with increasing pyrolysis temperature, but in the semi-closed system it increased slightly between 330 °C and 350 °C then remained relatively unchanged up to 450 °C. After, the S1/TOC ratio decreased almost to zero.

The geochemical differences between the two pyrolysis systems for samples MM15 and Y11 as above, and in Y2 in Guo et al. (2017), are briefly summarized here. For all three samples, the evolution in Tmax and HI showed similar trends for each pyrolysis systems (Fig. 2b, c, f, g). The TOC content of samples MM15 and Y2, with very high content of types I and II OM, respectively, decreased much more in the semi-closed system than in the closed system, which is related to differences in hydrocarbon expulsion (Figs. 2a and 3e in Guo et al., 2017); however, sample Y11 with lower TOC content, differed by 0.5 wt% or less (Fig. 2e). The S1/TOC ratios of all three samples, whether pyrolyzed in the semi-closed or closed system, were generally in the order MM15 > Y2 > Y11.

### 3.3. Characteristics of $N_2$ and $CO_2$ adsorption isotherms

#### 3.3.1. $N_2$ adsorption isotherms

Original samples MM15 and Y11 both have type IV $N_2$ adsorption isotherms, together with a type III hysteresis loop (Figs. 3a and 4a). Hysteresis loops are probably related to capillary condensation in mesopores; the type III loop may suggest slit-like pores in plate-like particle aggregates (Kuila and Prasad, 2013; Sing, 1985).

Considering the very high content both of clay minerals (Table 2) and OM in sample MM15—both more prone to compaction than other minerals in shale—sample MM15 was compacted at 80 MPa for 48 h without heating. The hysteresis loop of MM15 after compaction was steeper than the original at around the point of loop closure (Fig. 3a). After compaction, the $N_2$ adsorption capacity of MM15 decreased at maximum $P/P_0$ (Fig. 3a). The $N_2$ adsorptive capacity of the pyrolyzed samples in both systems largely decreased firstly at 330 °C compared to the original sample, then generally increased with increasing thermal maturity (Fig. 3c and d). In the closed system, $N_2$ adsorptive capacity of the pyrolyzed samples increased greatly between 330 °C and 380 °C, then increased little afterwards (Fig. 3c). By contrast, in the semi-closed system, only a small increase occurred between 330 °C and 380 °C, then increased noticeably from 380 °C to 500 °C (Fig. 3d). The shape of hysteresis loops differed little with increasing temperature for each pyrolysis system; therefore, the hysteresis loop of a single representative sample is shown for each pyrolysis system for comparison. It is evident in Fig. 3b that the hysteresis loop generated by samples in the semi-closed system is larger than in the closed system.

The adsorption capacity of pyrolyzed sample Y11, with relatively low TOC content and type III kerogen, was slightly less than the original sample at first (330 °C) in both pyrolysis systems, then slowly increased with increasing pyrolysis temperature in the closed system (Fig. 4b). In

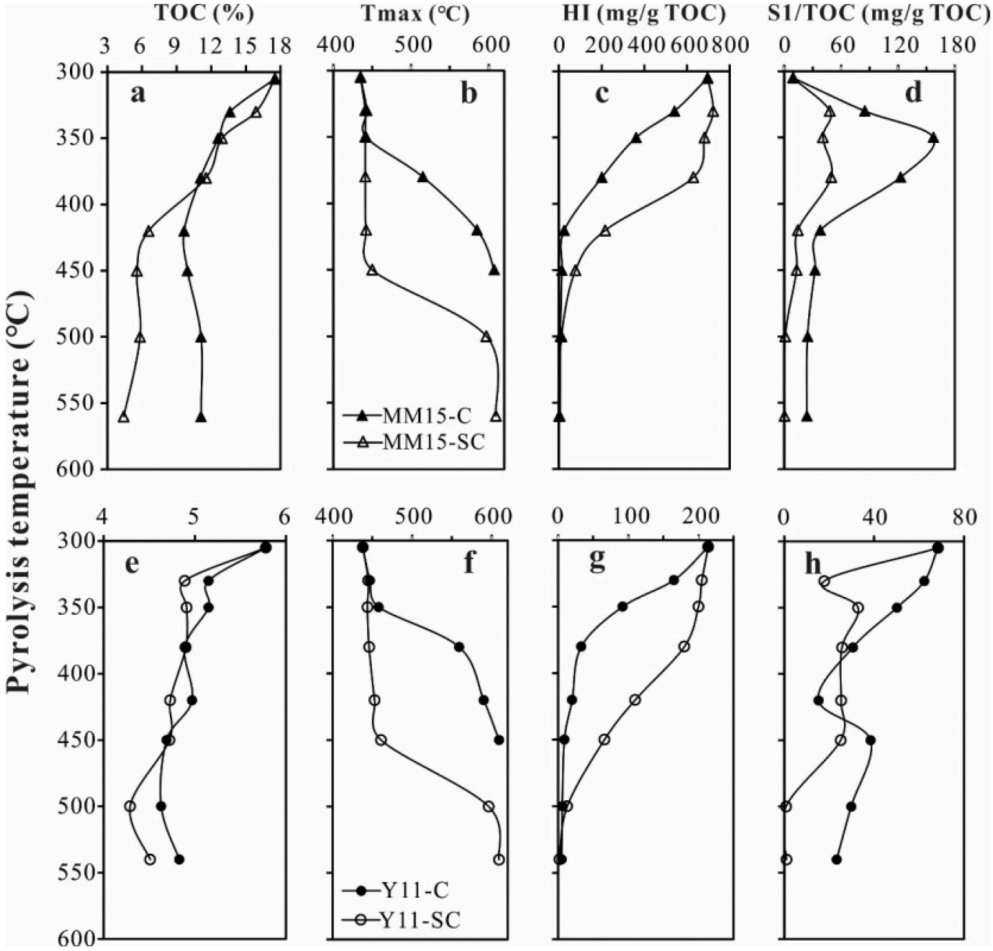


**Fig. 2.** Variation in geochemical characteristics with pyrolysis temperatures for: (a), (e) TOC; (b), (f) Tmax; (c), (g) HI; (d), (h) S1/TOC, where S1 is an indicator of free hydrocarbons in the sample (hydrocarbon/rock, mg/g). Panels (a)–(d) for sample MM15; panels (e)–(h) for sample Y11.

the semi-closed system, almost no change was observed between 330 °C and 450 °C, then increased sharply from 450 °C to 500 °C, then further increased slightly up to 540 °C (Fig. 4c).

### 3.3.2. $CO_2$ adsorption isotherms

The original and pyrolyzed samples of MM15 and Y11 have $CO_2$ adsorption isotherms of type I (Fig. 5). Similar to $N_2$ adsorption, the pyrolyzed samples adsorbed less $CO_2$ at 330 °C than the original sample, then the amount increased generally above 350 °C. The adsorptive capacity of pyrolyzed samples MM15 in the closed system showed a large increase between 380 °C and 420 °C (Fig. 5a). The adsorptive capacity in the semi-closed system greatly increased in the range 350–420 °C and 450–560 °C (Fig. 5b). Interestingly, compacted sample MM15-O-SC clearly adsorbed more $CO_2$ than the original (uncompacted) sample (Fig. 5b), unlike variations in $N_2$ adsorption before and after compaction (Fig. 3a).

The $CO_2$ adsorptive capacity of pyrolyzed samples of Y11 gradually increased up to 500 °C in the closed system (Fig. 5c). In the semi-closed system, the main increases were observed at 450–500 °C, 500–540 °C and 380–420 °C (Fig. 5d).

## 3.4. Pore-size distributions

### 3.4.1. Micropore volume distribution

The micropore volume distribution for the original and pyrolyzed MM15 and Y11 samples shows two main peaks at around 0.5 and 0.8 nm, with a minor peak between them (Figs. 6 and 7). Variations in pore volume of the peaks of the pyrolyzed samples with increasing temperature are similar for both systems, but show some differences, mainly with respect to the pyrolysis temperature interval, during which a large pore-volume increment was observed. Compacted sample MM15 showed a higher pore volume than the original sample at the 0.5 nm peak, but the 0.8 nm peak volume seems to have been little affected by compaction (Fig. 6c).

### 3.4.2. Meso- and macropore volume distributions

Distributions of pore volume in the 1.7–200 nm range were derived from the $N_2$ adsorption branch using the BJH model. The overall pore volume distributions in both the original and the pyrolyzed MM15 and Y11 samples resembled a unimodal pattern (Figs. 6 and 7). The major peak pore diameter covered a relatively wide range of 6–200 nm. The volume of pores below this range was very low, except for Y11 samples pyrolyzed in the semi-closed system at temperatures of 500–540 °C (Fig. 7d).

Except for these similarities, the three distinctly different samples (two in this study and one in Guo et al., 2017) exhibited notable disparities. Firstly, original sample MM15 containing abundant type I OM and clay minerals showed, after compaction without heating, a relatively slight but obvious decrease both in the major peak pore size (50–60 to ~40 nm, as shown by the arrowed, dashed line in Fig. 6f) and in the volume of pores >10 nm (Fig. 6f). Upon heating in the closed system, pore size increased greatly (100–200 nm, Fig. 6d). The size of pores in the semi-closed system peaked at about 100 nm at 330 °C, it then decreased gradually to about 40 nm up to 560 °C (shown by the arrowed, dashed line in Fig. 6e). The average pore width in the semi-closed system showed a similar evolutionary pattern (Table 1).

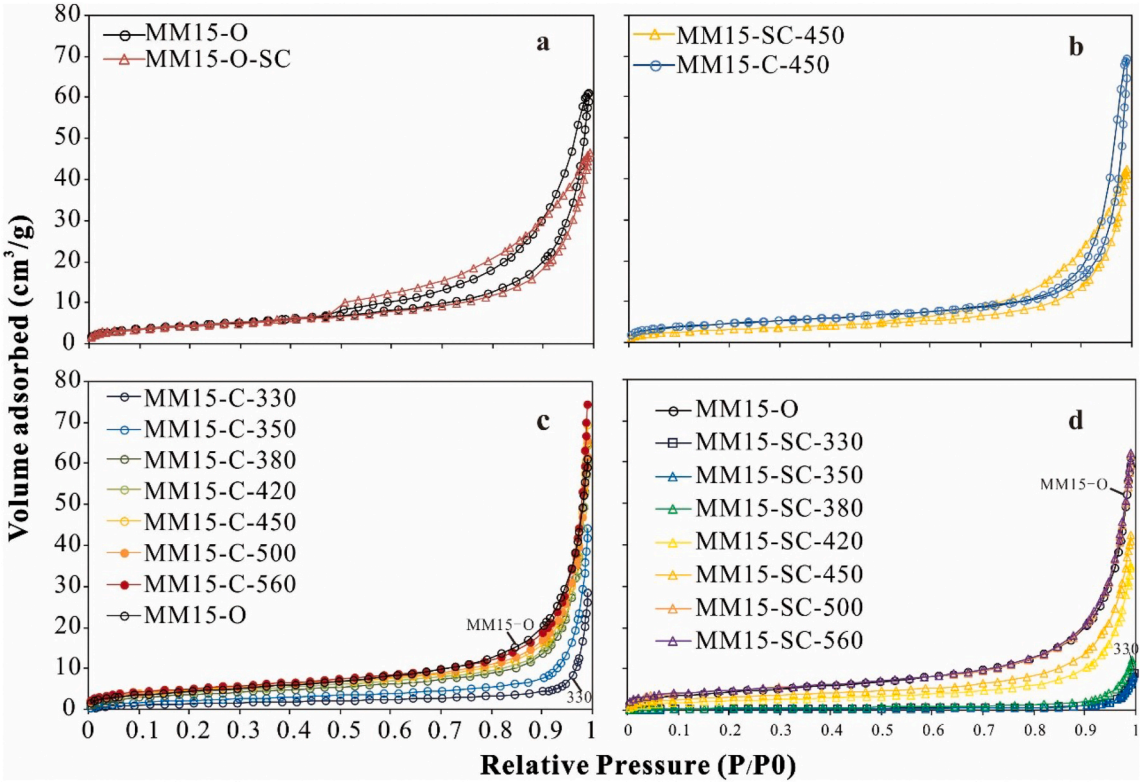


**Fig. 3.** (a) Low-pressure $N_2$ adsorption-desorption cycles of original sample MM15-O and compacted sample MM15-O-SC; (b) typical adsorption/desorption cycles of pyrolyzed samples from two pyrolysis systems; adsorption isotherms of pyrolyzed samples from (c) closed system and (d) semi-closed system.

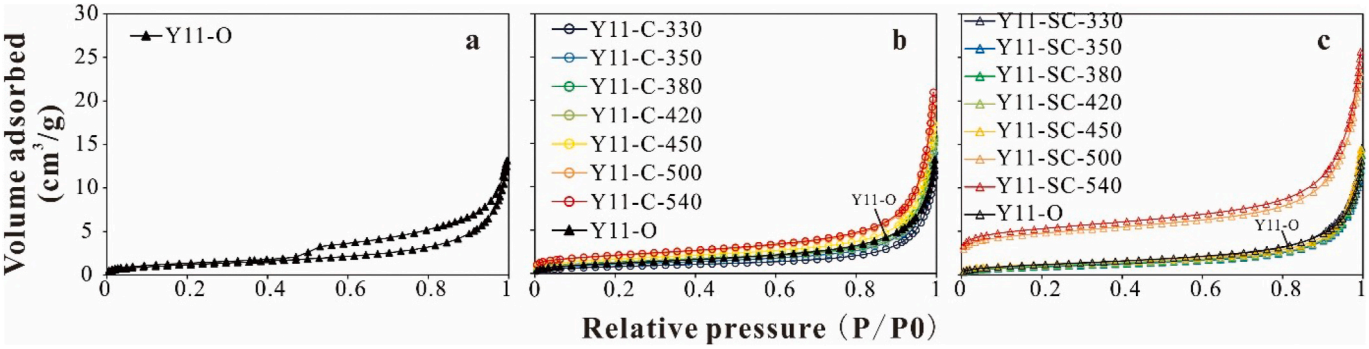


**Fig. 4.** (a) Low-pressure $N_2$ adsorption-desorption cycles for original sample Y11. Adsorption isotherms for pyrolyzed samples from (b) closed system, and (c) semi-closed system.

Secondly, in the closed system, pyrolyzed Y11 samples with a relatively low type III OM content showed no obvious variation in pore size at the major peak compared to the original sample (Fig. 7c). Samples pyrolyzed in the semi-closed system displayed similar results, with exceptions at 500 °C and 540 °C. The peak pore sizes for both samples were less at the major peak. A notable peak emerged (pore size < 6 nm: Fig. 7d), and the average pore width at 500 °C and 540 °C decreased from about 20 nm to about 15 nm (Table 1).

### 3.5. Pore-volume variations

Variations in the volume of pores in the different size ranges were obtained for pyrolyzed samples by combining the $N_2$ and $CO_2$ adsorption data (Table 1; Fig. 8a–d). Pores were classed as micropores (<2 nm diameter), mesopores (2–50 nm) and macropores (>50 nm) in accordance with International Union of Pure and Applied Chemistry recommendations. Pore volumes in pyrolyzed samples from the two systems generally showed an increasing trend at pyrolysis temperatures greater than 350 °C (Fig. 8). In addition, the micropore volumes in pyrolyzed MM15 samples from the two systems (Fig. 8d) were reasonably similar at the same pyrolysis temperatures. This was also observed on pyrolyzed samples of Y11 (Fig. 8h) for the two systems, but with substantial differences in pore-volume variation evident between the two samples.

The meso- and macropore volumes of pyrolyzed MM15 clearly differed significantly between two pyrolysis systems. A notable increase occurred in both macro- and mesopore volume in the semi-closed system between 380 °C and 500 °C. By contrast, this was most clearly seen between 330 °C and 380 °C in the closed system (Fig. 8b and c). Although the macropore volume in the closed system was always larger than in the semi-closed system, the difference between the two systems first increased with rising pyrolysis temperature (330 °C → 420 °C), then decreased, whereas the macropore volume in the closed system increased slightly (Fig. 8b). Mesopore volumes in the semi-closed system increased so much between 450 °C and 500 °C that they exceeded those

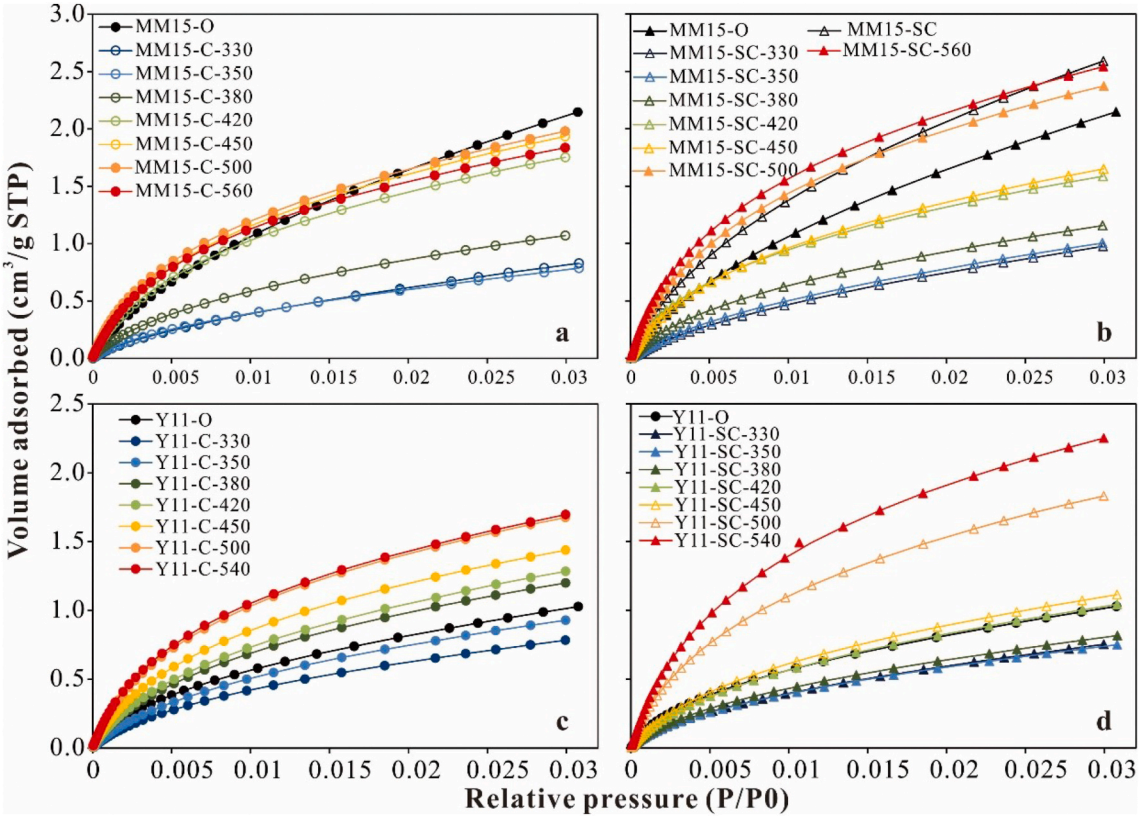


**Fig. 5.** Low-pressure CO2 adsorption isotherms for samples MM15 and Y11 pyrolyzed in: (a), (c) closed system; (b), (d) semi-closed system.

in the closed system (Fig. 8c). Overall, the total pore volumes of pyrolyzed samples in the semi-closed system were far less than those in the closed system below 420 °C, then approached the latter upon further heating (Fig. 8a).

In contrast, Y11 showed relatively small variation with pyrolyzing system (Fig. 8). The macropore volume was slightly smaller in the semi-closed than closed system (Fig. 8f); below 500 °C, this was also true for both meso- and micropore volumes (Fig. 8g and h).

### 3.6. Pore characteristics obtained from SEM observations

Based on OM morphology and origins, OM pores were subdivided into several subcategories: spongy, complex, shrinkage OM pores and OM bubble pores (Ko et al., 2016; Milliken et al., 2013). Complex OM pores had clearly discernible subparts, separated by partitions (Fig. 9C; Milliken et al., 2013). Spongy OM pores were generally at the nanometer scale, abundant and closely spaced (Fig. 9A; Ko et al., 2016). Shrinkage OM pores usually occurred between OM and mineral grains (Fig. 10B). They might be related to the post-experimental drops in confining pressure or the shrinkage of OM after OM expulsion (Ko et al., 2016; Wang et al., 2019). OM bubble pores were large pores developed in OMs with diameters from several hundreds of nanometers to a few micrometers (Fig. 11E). They were usually observed in the pyrolyzed samples in this study. Modified mineral pores were associated with both OM and mineral, with relic OM coating mineral grains (Ko et al., 2016).

The predominant pore types in raw sample MM15 consisted of the interparticle pores between minerals and the intra-clay platelet pores (Fig. 9A-B). The intra-clay platelet pores were smaller than the interparticle pores. Spongy and complex OM pores were evident, but less common (Fig. 9C). Although Y2 and MM15 had similar TOC content, their pore development degree was distinctly different. Sample Y2 was relatively poor in OM pores and inter-mineral pores (Fig. 9D-F) and only a few intra-clay platelet pores were observed (Fig. 9E). The different degree of pore development in Y2 and MM15 observed by FE-SEM was consistent with gas adsorption measurements (Figs. 9 and 13). Unlike MM15 and Y2, OM pores were the dominant pore type in the raw sample Y11 (Fig. 9G-I). Spongy OM pores were more common than complex pores. And sizes of OM pores were mainly in the 20–50 nm range. Mineral dissolution pores with mesopore size range were also observed (Fig. 9G). The larger mesopore volume than macropore volume observed under FE-SEM is also consistent with gas adsorption measurements (Fig. 9; Table 1).

At the oil generation stage (350 °C), OM bubble pores were common in pyrolyzed samples of MM15 (Fig. 10A, B). Some shrinkage pores or microfractures were observed between the interfaces of OM and minerals (Fig. 10B). Most of the original inter-mineral and intra-mineral pores had disappeared; it is likely that they had been filled by residual petroleum (Fig. 10C-E). By the dry gas stage (500 °C), most hydrocarbon fluids had been expelled, resulting in a significant increase in the abundance of relatively large modified mineral pores in both pyrolysis systems (Fig. 10G-L). Round OM pores of size 15–75 nm distributed in the matrix and intra-clay platelet pores (main size range of 30–60 nm) were only occasionally observed in samples pyrolyzed in the closed system (Fig. 10F, G). Spongy OM pores were uncommon and difficult to discern in samples at the dry gas stage in the semi-closed pyrolysis system (Fig. 10J-L).

As with pyrolyzed samples of Y2 having high type II kerogen content, at the oil generation stage (350 °C), shrinkage-related pores were commonly observed especially between mineral grains and OM at the oil generation stage for the semi-closed system (Fig. 11A, C). Inter-particle pores between clay minerals and other minerals, mineral dissolution pores were observed but were less common. Overall, more extensive pore development was observed in the pyrolyzed sample from the closed system than from the semi-closed system. Besides the shrinkage pores and dissolution pores, modified mineral pores and OM bubble pores were also observed (Fig. 11D-F). This might be related to the higher

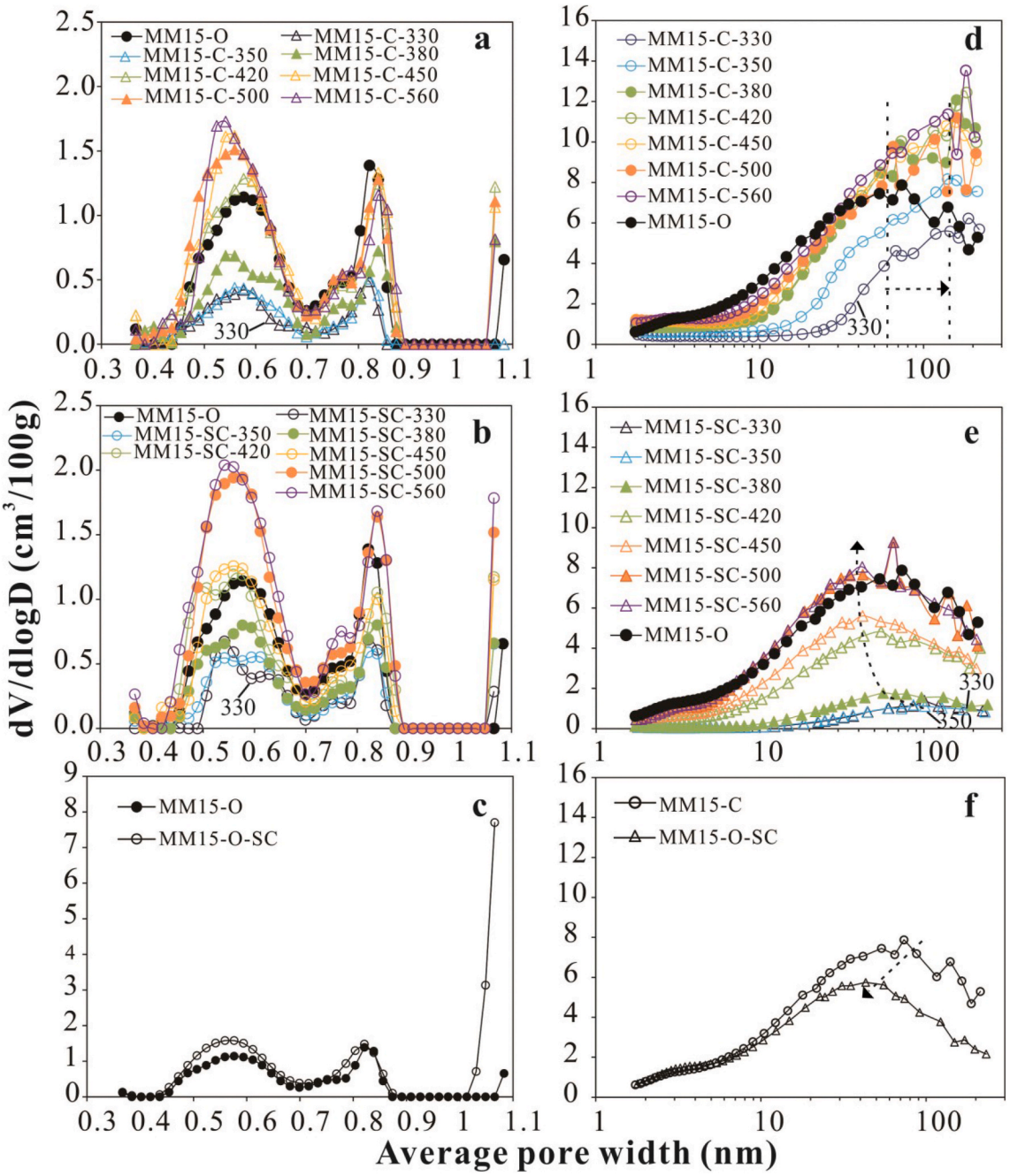


**Fig. 6.** Volume distribution with average pore width, from $CO_2$ and $N_2$ adsorption isotherms for: (a), (d) closed system; (b), (e) semi-closed system; (c), (f) unheated sample MM15-O and compacted sample MM15-O-SC.

thermal maturity from the closed system (VRo = 0.87%) than from the semi-closed system (VRo = 0.70%) (Guo et al., 2017). It should be noted that most of the OM was still non-porous at this stage. The modified mineral pores and OM bubble pores were commonly observed between OM and mineral grains (mostly clay minerals). Intra-clay platelet pores resulting from dehydration were uncommon in Y2 at this stage; this might be related to the infilling of these pores with petroleum, which was similar to MM15-350. At the dry gas stage, modified mineral pores and OM bubble pores were the dominant pore types for the closed system. Intra-clay platelet pores were less common (Fig. 11H). Although the pyrolyzed samples were at the high-to-over mature stage (VRo = 1.49%–1.95%), some fractions of OM were still non-porous (Fig. 11I). The size of pores in OM filling between clay mineral layers was tens to a hundred nanometers (Fig. 11G). Modified mineral pores were larger and the pore size was 100–500 nm (Fig. 11G, H). The size of OM bubble pores was mainly hundreds of nanometers and, with some up to 5 μm. A few intra-clay platelet pores without relict OM were several hundreds of nanometers in size (Fig. 11H). As with the closed system, modified mineral pores and OM bubble pores were the predominant pore types. Intra-clay platelet pores were also present (Fig. 11K). Unlike the closed system, complex and spongy OM pores were common for the semi-closed system (Fig. 11J-L). These pores were either connected or isolated, and irregular in shape, with diameters ranging from 100 to 700 nm (Fig. 11K, L). Spongy OM pores were rounded or subrounded, with diameters ranging from 20 to 90 nm (most in the 20–40 nm range).

In terms of pyrolyzed samples of Y11 having type III kerogen, at the oil generation stage, pores associated with OM included OM bubble pores, spongy OM pores, complex OM pores and fractures in OM

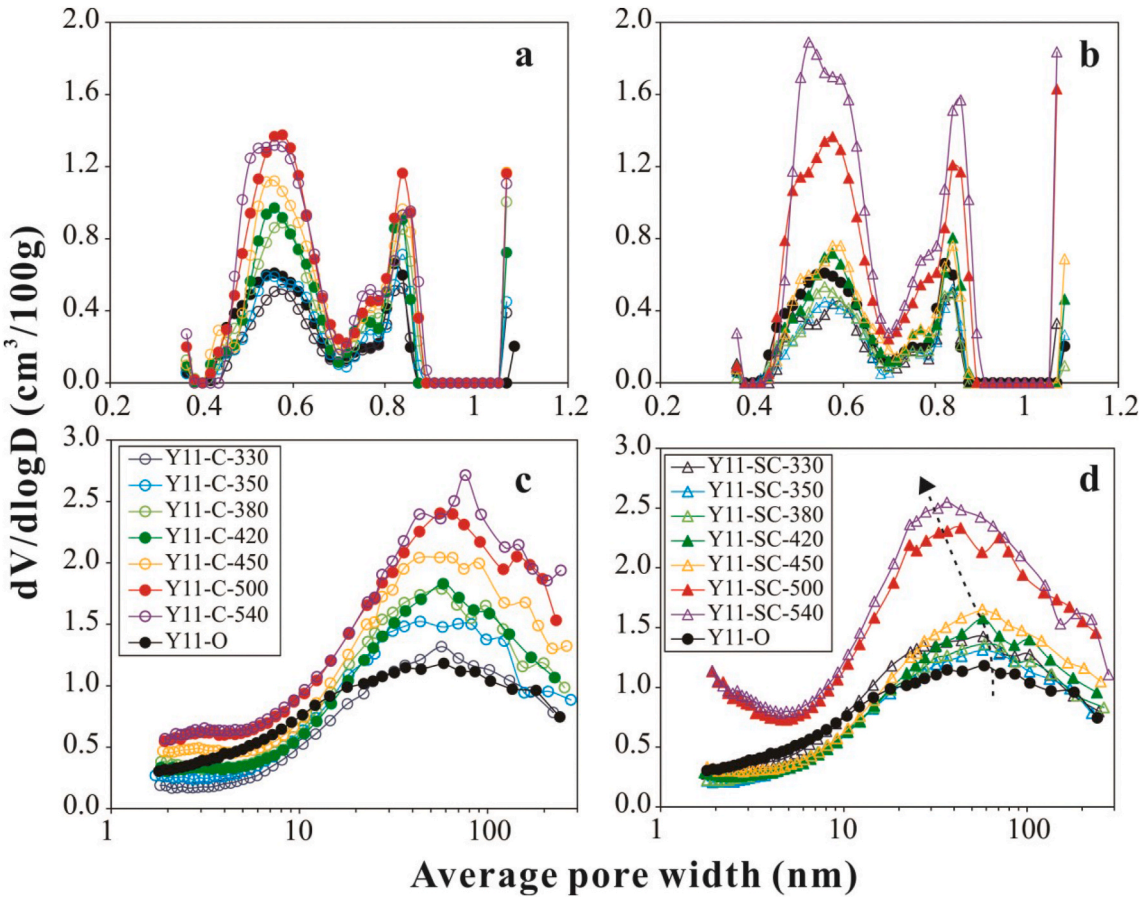


**Fig. 7.** Volume distribution with average pore width, from $CO_2$ and $N_2$ adsorption isotherms for pyrolyzed samples and original sample Y11: (a), (c) closed system; and (b), (d) semi-closed system. a and c share the same legend, and b and d share the same legend.

(Fig. 12A, B, F). Spongy OM pores were predominant (Fig. 12A, F). The other pore type was intra-clay platelet pore (Fig. 12C-D). Mineral dissolution was also observed, but no pores were seen in the minerals under FE-SEM (Fig. 12E). Some OM with irregular shapes observed between minerals and particulate OM (inertinite or vitrinite maceral) were non-porous (Fig. 12$B_1$, E, F). There was little difference between the two different pyrolysis systems for samples at the oil generation stage. At the dry gas stage, the dominant pore types for the closed system included modified mineral pore, OM bubble pore, spongy OM pore and complex OM pore (Fig. 12G, I-J, L). Diameters of the OM pores mainly ranged between 30 and 200 nm, although the OM bubble pores were up to several micrometers in size (Fig. 12J). Other pore types included intra-clay platelet pores between 20 and 200 nm (main range 20–90 nm) and mineral dissolution pores (Fig. 12G-H, K-L). Pore types in the sample pyrolyzed in the semi-closed system were similar to those from the closed system (Fig. 12M-Q), but complex OM pores were more prevalent and bubble pores were fewer and smaller in the semi-closed system. Complex OM pores had rounded or elliptical shapes with diameter range of 8–80 nm (main peak 10–50 nm). The OM pore diameters were much smaller than from the closed system. Large fractures were evident in the porous OM (Fig. 12O). At the dry gas stage, micrometer-sized particulate OM was still non-porous (Fig. 12R).

## 4. Discussion

Elucidation of the coupling of OM changes with pore development is significant for at least two important reasons. One is to help to gain insight into key pore-development processes and their relationship with OM transformation and expulsion; the other lies in applying meaningful constraints to models for predicting shale porosity based on the OM compositions of shale at different maturities. The former issue has been discussed in previous pyrolysis studies on shale pore development, but by contrast, the latter has received much less attention. Even for the first issue, comparisons of pore development in shales of different compositions have been performed only in a few studies (Cavelan et al., 2019; Ko et al., 2018; Liu et al., 2017a,b,c). Pore evolutionary trends of three pyrolyzed sample series, one obtained by Guo et al. (2017) and two in the present study, are unique not only with respect to the shale sample properties but also the pyrolysis conditions (Fig. 13). It has been found that variations in OM transformation and expulsion processes—probably related to pyrolysis conditions and the original OM content and type—have a significant impact on shale pore development, which would be explained in detail in section 4.1.2.

Our previous study discussed the effect of pyrolysis conditions (mainly lithostatic pressure) on OM maturation, generation, expulsion and composition of oil, as well as the development of pores of different size based on observations of pyrolyzed Y2 samples containing abundant type II OM (Guo et al., 2017). The following discussion emphasizes the impact of OM compositions on pore development process and extent, by combining the results of the three samples.

### 4.1. Pore development processes related to OM evolution in shale

The evolution of OM and pore volume occurred in four main stages during pyrolysis (Fig. 13).

Stage I: At the early oil generation stage, the three samples series, whether from the semi-closed or closed system, all showed varying reductions of TOC and pore volume. This phenomenon has previously been observed and demonstrated in many oil shale samples at the oil generation stage (Chen and Xiao, 2014; Mastalerz et al., 2013; Valenza

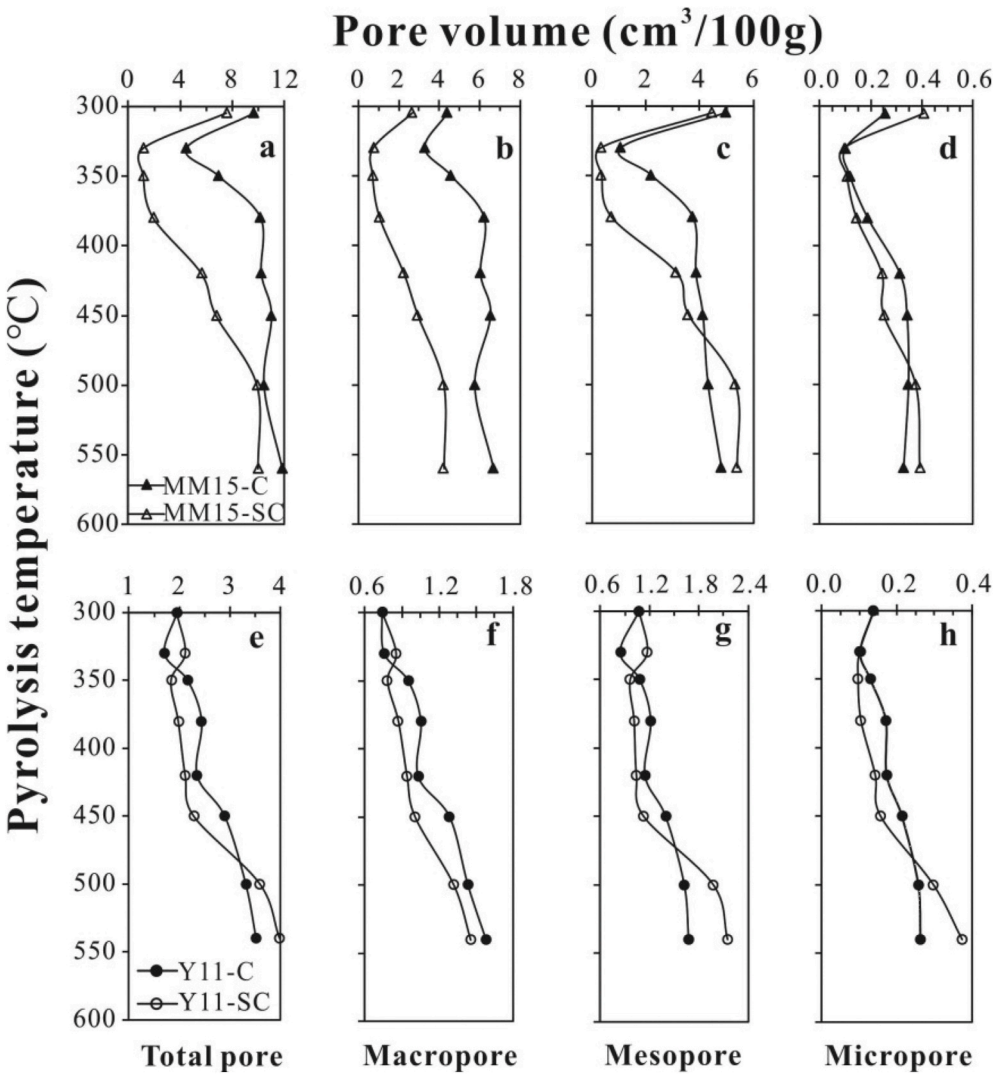


**Fig. 8.** Volume variation for pyrolyzed samples of MM15 and Y11: (a), (e) total pores; (b), (f) macropores; (c), (g) mesopores; and (d), (h) micropores.(C = closed system; SC = semi-closed system).

et al., 2013) resulting from occlusion or infilling of pores in shale by residual bitumen.

Stage II: With further thermal evolution, the cracking of residual bitumen into oil, cracking of oil and expulsion of generated oil lead to pore volume increase but TOC reduction. This is more apparent in shale with type I and II OM and higher TOC content (Fig. 13a, b, d, e).

Stage $III_1$: The early condensate and wet gas stage, in which the increment of pore volume is related to significant cracking of the oil into gas and lighter hydrocarbons and resulted hydrocarbon expulsion.

Stage $III_2$: The middle-to-late condensate and wet gas stage, in which the lighter hydrocarbons are mainly cracked into wet gas and condensate components. The TOC values for pyrolyzed samples are nearly constant throughout this stage, suggesting that oil expulsion, rather than gas expulsion, is the main cause for TOC reduction in shale. During this stage, pore volume of shale increased little for the semi-closed system, While, pore volume of shale samples with type II and III OM from the closed system showed some increase (Fig. 13).

Stage IV: The dry gas stage, in which the wet gas and condensate are cracked into methane. The TOC and pore volume of pyrolyzed shale samples showed little change during this stage.

#### 4.1.1. *Effect of residual bitumen on pore volume*

Gas adsorption and Hg intrusion measurements reported for geological shale samples at different maturities (Mastalerz et al., 2013) suggest that once the shale has evolved into the oil window, it displays a notable decrease of pore volume due to the oil and solid bitumen filling primary pores. Results from the present study also showed that all three samples displayed different degrees of pore-volume decrease almost independently of pyrolysis system. This was most evident for samples MM15 and Y2 with high TOC content (Fig. 13).

Since the presence of residual oil is responsible for the decrease of shale porosity, it is likely that the amount of residual oil may have a close relationship with reduced pore volume. For the three samples pyrolyzed in the closed system, maximal decrease of total pore volume (ΔTPV = original pore volume (Vo) - the lowest pore volume (Vmin) obtained at 330 or 350 °C) was 5.21 $cm^3$/100 g for sample MM15, 0.37 $cm^3$/100 g for sample Y2 and 0.25 $cm^3$/100 g for sample Y11 (Table 3). The ratio of pore-volume decrease (ΔTPV) to original pore volume (Vo), i.e. DR, was 54%, 26% and 7% for MM15, Y2 and Y11, respectively (Table 3).

The differences in S1 (ΔS1, Table 3) between pyrolyzed samples at 330/350 °C (at which the lowest pore volume was obtained) and corresponding original samples were 9.92, 16.46 and −0.71 mg/g for MM15, Y2 and Y11, respectively. Although their ΔS1 values explain the relatively large DR of TPV for MM15 and Y2 compared to sample Y11, the ΔS1 for Y2 was higher than for MM15, whereas the DR of Y2 was

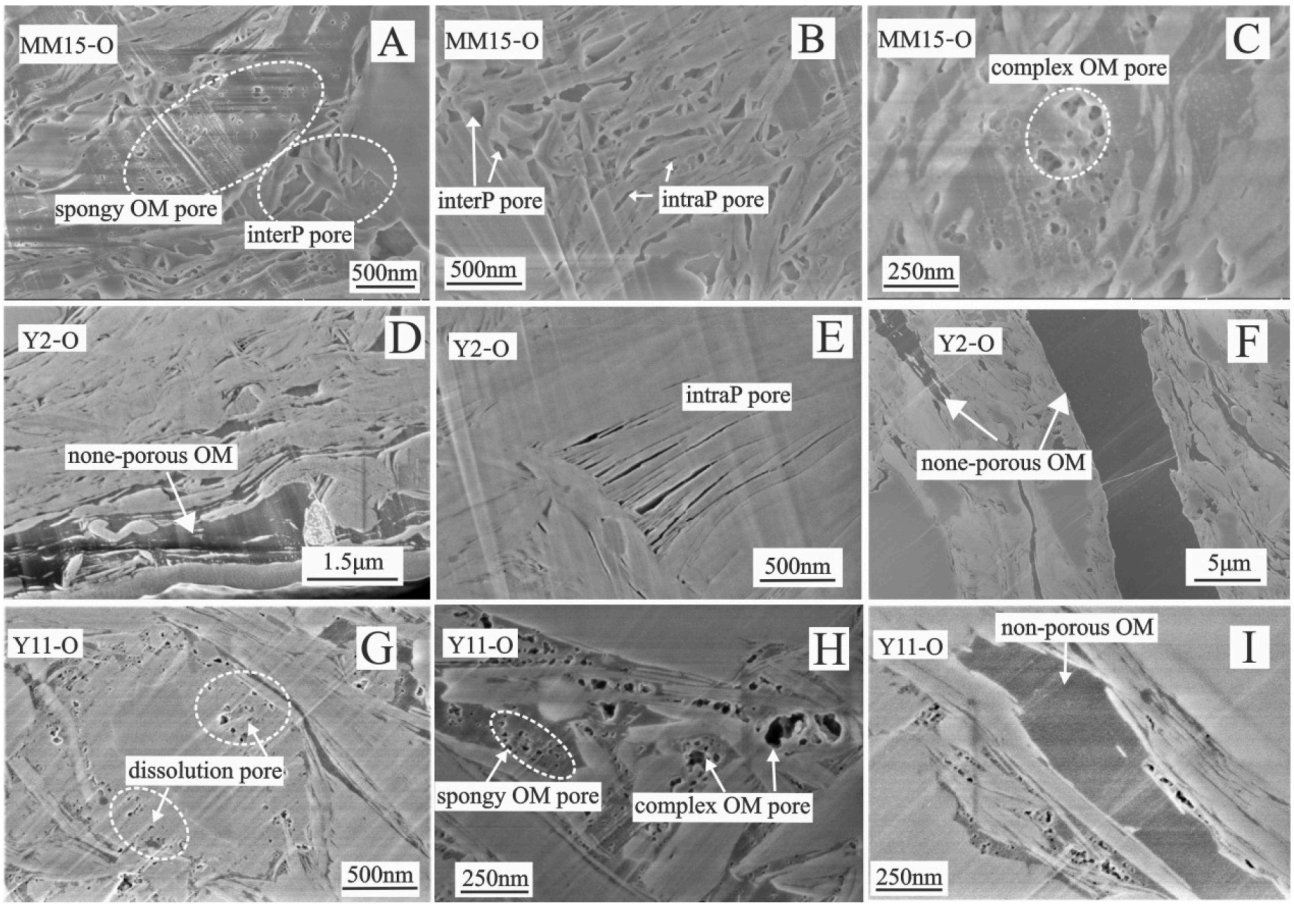


**Fig. 9.** FE-SME images showing the pore types in the raw shale samples. (A) Spongy OM pores and interP (inter-particle) pores between minerals in MM15-O; (B) interP pores between minerals and intra-clay platelet pores in MM15-O; (C) complex OM pores in MM15-O; (D), (F) non-porous OM in Y2–O; (E) intra-clay platelet pores in Y2–O; (G) mineral dissolution pores in Y11–O; (H) spongy and complex OM pores in Y11–O; (I) non-porous OM and spongy OM pores in Y11–O.

lower. It seems like that ΔS1, which includes only the free hydrocarbons of lower boiling point, is not the main factor in pore volume reduction. It is known that some extractable hydrocarbons with higher boiling point belong to S2. As the OM type in MM15 was of better quality than that in Y2, and since they both had similar TOC content, MM15 would be expected to contain a greater amount of heavier extractable OM than Y2 (Pepper and Corvi, 1995). Such heavier hydrocarbons would also occupy and clog pore throats, lowering the measured pore volume (Wei et al., 2014; Zargari et al., 2015). Therefore, the OM type and content could be the main factors influencing the reduced pore volume at the oil generation stage.

One similarity between the three shale samples was the different extents of micro-, meso- and macropore volume reduction. Notably, the mesopore volume of pyrolyzed samples of MM15 showed the largest reduction, followed by macropore, then micropore volume reduction (Fig. 14a). On a relative scale (Fig. 14b), the reduction of mesopore volume was also the largest, followed by micropore, then macropore volume. For the two samples from the Chang7 Member, the reductions of pore volume were in the order micropores > mesopores > macropores (on a relative scale, Fig. 14b). Relatively, for each pore-size class, the reductions of pore volume were in the order MM15 > Y2 > Y11 (Fig. 14b). It is concluded that residual bitumen in shale had the greatest impact on micropores, compared with the meso- and macro-pores; and shale of type I OM produced a greater reduction in the volume of pores in all size classes than shale sample of type II OM. The TOC content of Y11 was about 10 wt% less than for Y2 and MM15. The lower TOC content of Y11 led to the lower residual bitumen content. Therefore, the lower DR in Y11 than in Y2 is related to both OM type and content. A comparative study of pore volumes of original and solvent-extracted Chang7 shales (Li et al., 2016) also suggested that residual bitumen affected the micropore volume to a larger extent than the meso- and macropore volume. Furthermore, that study showed an approximately positive correlation between the amount of extractable OM in the shale and an increase in pore volume.

By contrast, another study observed that, after solvent extraction using dichloromethane and toluene, shale samples at low thermal maturity showed an increase in micropore volume only, and in shale samples of different maturity, micro- and mesopores clearly increased in pore area (Wei et al., 2014). When the pore throat is occupied by residual oil or bitumen, $N_2$ may be obstructed from entering the pores when attempting to measure pore volume and area by low-pressure $N_2$ adsorption. The measured pore volume is therefore smaller than the actual volume. However, the removal of oil/bitumen also enlarged the pore space to larger pores that could not be measured by $N_2$ adsorption (Wei et al., 2014), which may be responsible for the sole micropore volume increase for shale samples at low thermal maturity.

#### 4.1.2. *Effect of hydrocarbon generation and expulsion on pore development*

After reaching their minimum value, the pore volume of pyrolyzed samples generally increase with further maturation, but to different extents in each case. During the thermal evolution of shale samples, OM decomposition and expulsion increase pore volume, and dehydration and decarboxylation of clay minerals reduce pore volume (Chen and Xiao, 2014; Noyan et al., 2006). However, previous FE-SEM observation has shown that intra-clay platelet pores became larger at pyrolysis temperatures below 350 °C, and little or no change when the

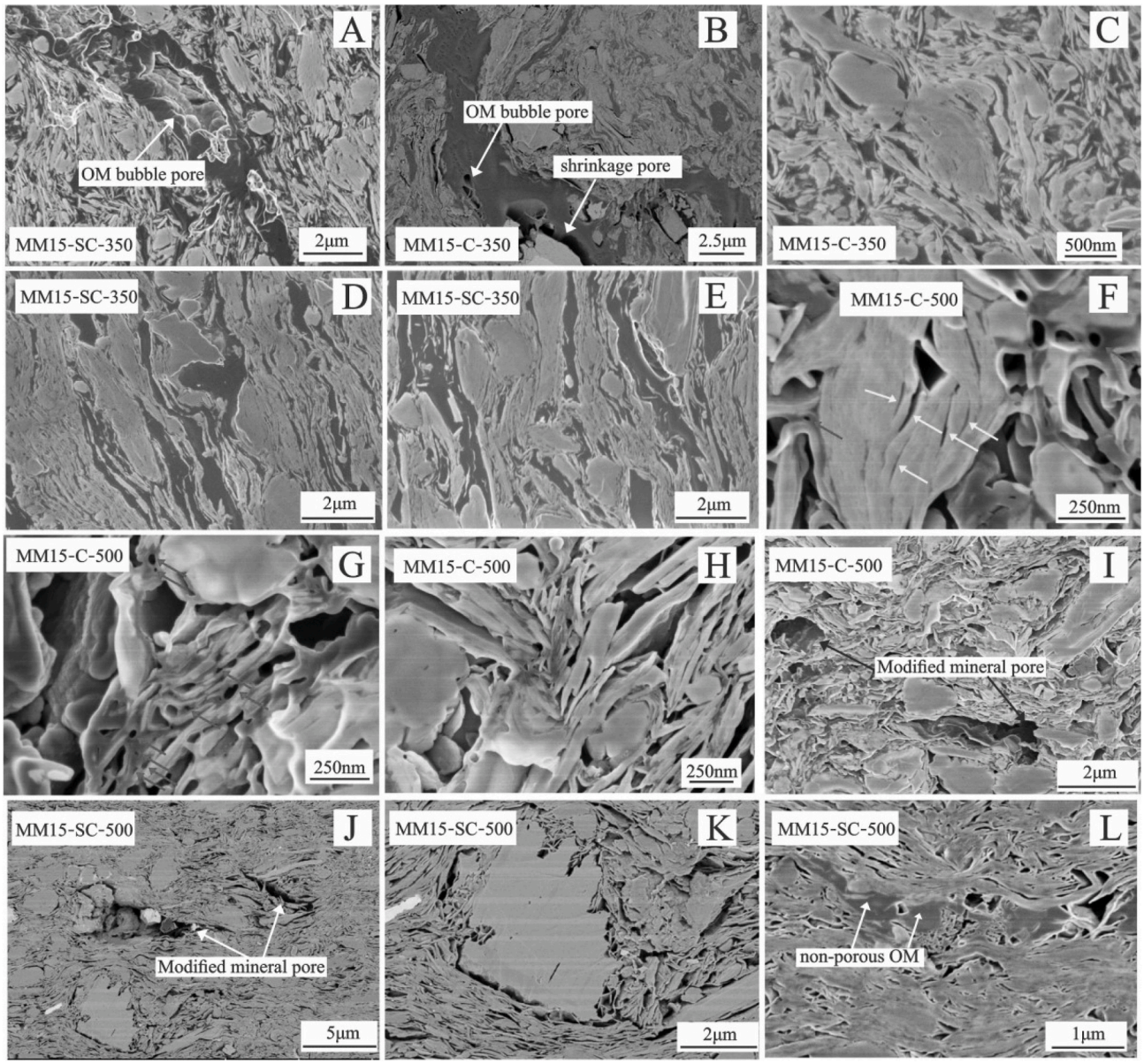


**Fig. 10.** FE-SME images of pore types in pyrolyzed samples of MM15 at the oil generation stage and dry gas stage. (A) OM bubble pores; (B), (E) OM bubble pores and shrinkage OM pores; (C)–(E) primary inter-mineral pores and OM pores had all been filled with OM; (F), (G) intra-clay platelet pores (yellow arrows) and rounded OM pores (red arrows); (F)–(K) modified mineral pores; (L) modified mineral pores and non-porous OM.

temperature was higher than 350 °C (Cui et al., 2013; Wu et al., 2015). The contribution of mineral dissolution pores to the total increase in pore volume was small (about 10%) when compared with the clay mineral pore and OM pore (Wu et al., 2015). For the OM-rich pyrolyzed samples in the present study, FE-SEM observations showed that the clay mineral pores and mineral dissolution pores were mostly occupied by petroleum at the oil generation stage (pyrolysis temperature 350 °C; Figs. 12L and 10A-E). The observed intra-clay platelet pore volume increase reported in other studies might have also occurred in pyrolyzed samples in the present study, but filled with petroleum, as the TOC content of pyrolyzed samples in this work exceeded that in Wu et al. (2015). The TOC content of the raw sample and of the sample pyrolyzed at 350 °C in Wu et al. (2015) were 2.23% and 0.32%, respectively. Pore volume increase mainly occurred when the pyrolysis temperature was higher than 350 °C (Fig. 13). Therefore, the observed pore development was attributed to relatively large hydrocarbon expulsion as a result of significant secondary cracking of previously generated bitumen or oil from thermal degradation of the kerogen originally in the shale at pyrolysis temperatures higher than 350 °C. The process of hydrocarbon expulsion is complicated, since it is associated with both OM type and content; however, the net hydrocarbon expulsion is directly reflected by a decrease in TOC content. The reduction is much less for a closed system than for a semi-closed system, which is related to relatively rapid cracking of residual bitumen when subjected to low fluid pressure (Guo et al., 2017). Therefore, high thermal-maturity samples from the semi-closed system were chosen to illustrate the effect of hydrocarbon generation and expulsion on pore volume.

The decrease of TOC content is coupled with evidently increased pore volume for all three samples pyrolyzed in the semi-closed system, corresponding to maturities from Ro 0.7%–1.49%. Decreases from 12.93 wt% to 5.83 wt% (MM15), from 20.33 wt% to 12.72 wt% (Y2) and from 4.41 wt% to 3.79 wt% (Y11) were mainly observed between 350 °C and 500 °C (Fig. 13a–c; Table 1). By contrast, total pore volumes increased from 1.18 $cm^3$/100 g to 9.91 $cm^3$/100 g (an increase of 8.73 $cm^3$/100 g), from 1.09 $cm^3$/100 g to 3.60 $cm^3$/100 g (increased by 2.51 $cm^3$/100 g), and from 1.84 $cm^3$/100 g to 3.59 $cm^3$/100 g (increased by

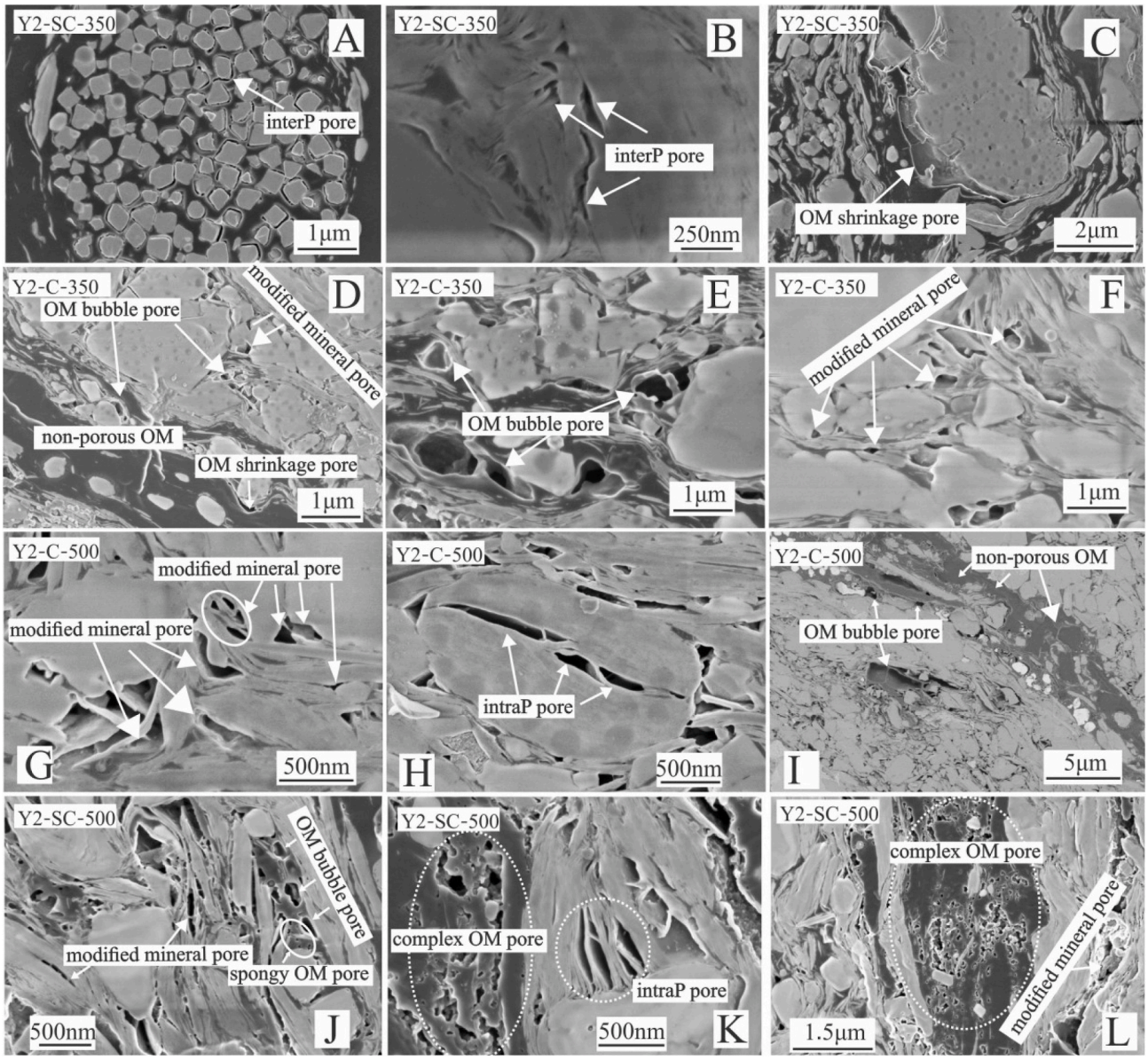


**Fig. 11.** FE-SEM images showing pore types in the pyrolyzed samples of Y2 at the oil generation stage and dry gas stage: (A) inter-particle pores between OM and pyrites; (B) inter-particle pores between minerals; (C) OM shrinkage pores; (D) modified mineral pores, OM bubble pores, shrinkage OM pores and non-porous OM; (E) OM bubble pores; (F) modified mineral pores; (G) modified mineral pores; (H) intra-particle pores; (I) OM bubble pores and non-porous OM; (J) OM bubble pores, spongy OM pores and modified mineral pores; (K) complex OM pores and intra-clay platelet pores; (L) complex OM pores and modified mineral pores.

1.75 $cm^3$/100 g), for samples MM15, Y2 and Y11, respectively. It is speculated that a large mass loss of OM resulted in a large increase of total pore volume in shale (best displayed by sample MM15 with type I OM). And a slight decrease of type II/III OM (sample Y11) was related to a notable increase in total pore volume. However, although a similar loss of type II OM for Y2 with MM15, would not cause a large pore volume increase. Thus, the decrease in TOC content was not proportional to pore volume increase measured by gas adsorption in the studied samples. The reason could be that macropores larger than the measurement range of low pressure $N_2$ gas adsorption were present in the matured shale samples. Liu et al. (2019) conducted the thermal simulation of a shale sample from Yanchang Formation by using the same pyrolysis simulation equipment as this work and measured pore volume by combining low-pressure gas adsorption, mercury intrusion and helium pycnometry. Their work showed that abundant macropores larger than the measurement scope of $N_2$ gas adsorption (0.23–1.63 $cm^3$/100 g) were present in matured samples. For different shale samples, the proportion of these large pores is likely to be different. According to the FE-SEM observation, abundant primary pores were filled with petroleum at the oil generation stage in both pyrolysis systems for MM15 with type I OM (Fig. 9A, B; 10 A-E). However, at the dry gas stage, most of the fluids have been expelled, resulting in a significant apparent increase in modified mineral pore volume (Fig. 10F-L). For Y2 with type II OM, the predominant pore types were modified mineral pore, fractures, OM bubble pore, complex OM pore and spongy OM pore at the dry gas stage (Fig. 11). At this stage, although pore types of Y11 with type III OM were similar to that of Y2, the proportion of complex OM pore and spongy OM pore was larger and the pore diameter was smaller for Y11. For shale sample MM15 of type I OM, the OM tended to generate more oil per TOC content than Y2 with type II OM (Behar et al., 1997). For Y11 of type II/III OM, the amount of product generated per TOC content should comprise a lower ratio of liquid hydrocarbon and a higher ratio of gas hydrocarbon during thermal evolution when compared to samples with type I and II (Behar et al., 1997; Hunt, 1991). Previous work has shown

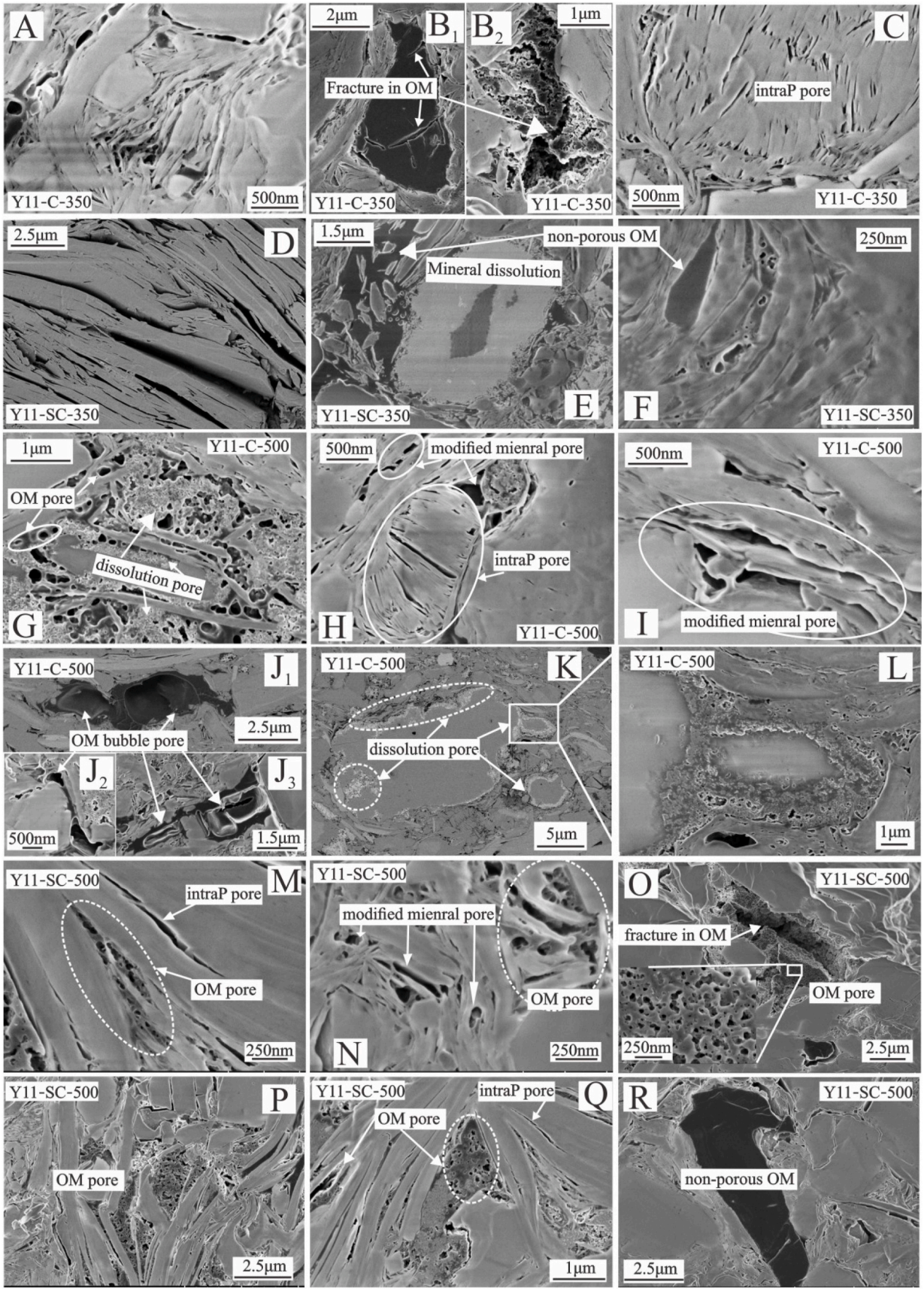


**Fig. 12.** FE-SEM images of the pyrolyzed samples of Y11 at the oil generation and dry gas stages: (A) OM bubble pores and OM pores distributed between clay layers; ($B_1$) non-porous OM with fractures; ($B_2$) complex OM pores and fractures; (C), (D) intra-clay platelet pores; (E) mineral dissolution and non-porous OM; (F) non-porous OM and spongy OM.

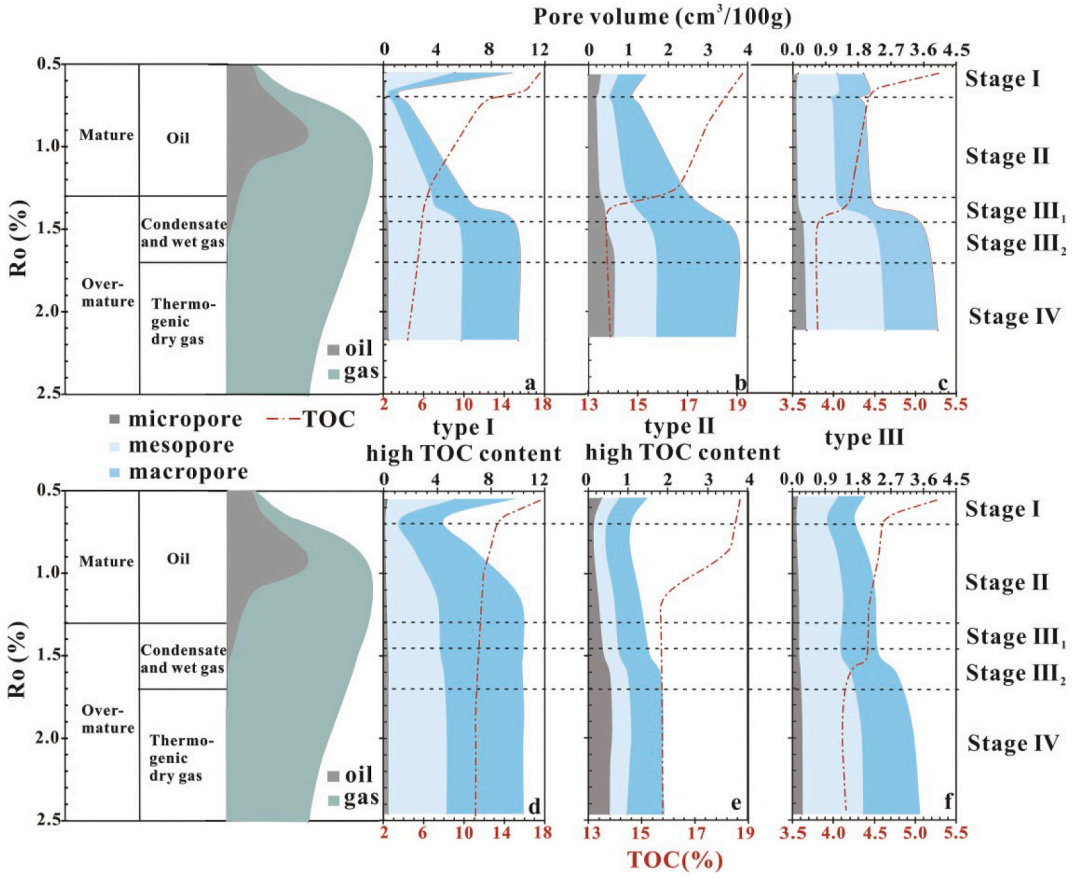


**Fig. 13.** Evolution of pore volume and TOC in shales with increasing thermal maturity (modified after Mastalerz et al., 2013): (a)–(c) semi-closed pyrolysis system; (d)–(f) closed system. Red Lines represent TOC content. In geological situations, in addition to temperature and time, OM transformation could be influenced by other geological factors, for example, overpressure (Carr, 2003; Hao et al., 2007), liptinite content (Peters et al., 2018), and organic-inorganic interactions (Seewald et al., 2000; Yang et al., 2018). Therefore, the pore evolution with thermal maturity of shale samples with different OM types is qualitative. For the convenience of comparison, the Ro values for both pyrolysis systems of Y2 published previously were used as thermal indicators in the model (Guo et al., 2017). (For interpretation of the references to colour in this figure legend, the reader is referred to the Web version of this article.)

**Table 3**
S1 increase and maximal pore volume decrease of pyrolyzed samples at the oil generation stage.

| Sample | ΔS1 (mg/g rock) | ΔTPV ($cm^3$/100 g) | DR (%) |
|---|---|---|---|
| MM15-C-330 | 9.92 | 5.21 | 53.65 |
| Y2–C-350 | 16.46 | 0.38 | 26.31 |
| Y11–C-330 | −0.71 | 0.25 | 6.81 |

$\Delta S1 = S1$ of sample with lowest pore volume ($S1_{Vmin}$) – S1 of the corresponding original sample ($S1_O$).
$\Delta TPV$ = total pore volume of original sample ($V_O$) – lowest pore volume ($V_{min}$).
DR (decrease ratio) = $\Delta TPV/V_O \times 100\%$.

that the oil devolatilization facilitated the formation of fractures and pores with larger diameter associated in OM, and the exsolution of gas from OM formed bubbles with smaller diameters in OM (Loucks et al., 2009). The diameters of OM bubble pores and modified mineral pores were mostly in the macropore range. Thus, oil generative shale with type I and II OM readily generates large-diameter pores, and gas generative shale of type III OM readily produces smaller-diameter pores as a result of hydrocarbon generation and expulsion during thermal maturation.

#### 4.1.3. Influence of pressure on pore development

Previous studies have shown that the porosity of shales is greatly reduced by compaction during the sedimentation and diagenesis processes (Dewhurst et al., 1999). At the catagenesis stage the pore volume is further reduced by mineral transformation and pressure dissolution (Pommer and Milliken, 2015). Kuila and Prasad (2013) found that compacting clay minerals at different pressures easily reduced pores larger than 5 nm. Compaction experiments applying different lithostatic and hydrostatic pressures on shale and coal have indicated that pores larger than 100 nm are reduced in size to different extents (Mastalerz et al., 2018). In muddy shales pyrolyzed at high pressure, micrometer-scale capillary pores and megapores decreased substantially in size, and in one case porosity fell from 14.39% to 7.3% when the pressure was increased from 50 MPa to 100 MPa (Ji et al., 2017).

Compared to the geological shale samples, shale samples matured in the laboratory were compacted for just 48 h in this work. However, the impact of 48 h-compaction on the pore volume of original MM15 was great (Table 1; Fig. 6f). About 40% of the macropore volume of the original sample of MM15 was reduced by compaction and the micropore volume increased, indicating that larger pores may have been compacted into smaller pores.

During thermal simulation in the semi-closed system, the overburden pressure exerted from the top down also influenced pore development. FE-SEM observation showed that OM pore types were different for the two pyrolysis systems for Y2 and Y11. Except for the large OM bubble pores in Y2-SC-500, abundant spongy and complex OM pores with diameter ranges of 20–90 nm and 100–700 nm were present. While, it was difficult to find the spongy and complex OM pores in Y2–C-500, only significantly large OM bubble pores (hundreds of nanometers to several micrometers in diameter) were commonly observed (Fig. 11). The similar phenomenon was found in Y11-SC-500 and Y11–C-500

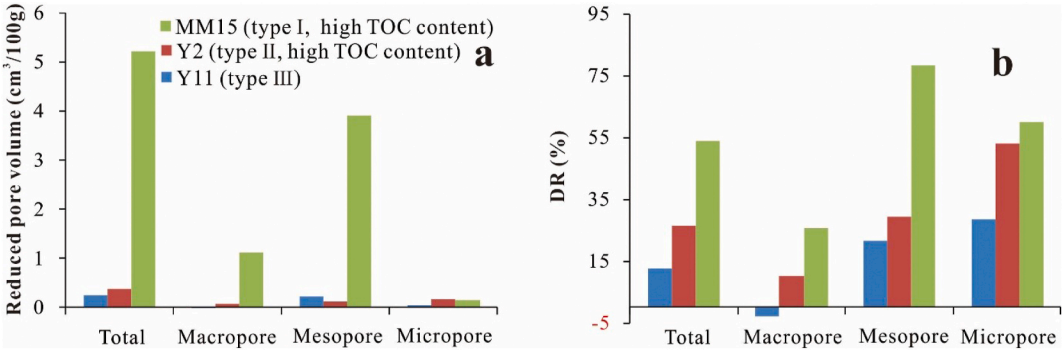


**Fig. 14.** Effect of residual bitumen on pore volume in shales with different OM compositions from closed system pyrolysis at the oil generation stage: (a) Reduced volumes of total pores, macropores, mesopores and micropores. Reduced pore volume = (pore volume in original sample) – (smallest pore volume of pyrolyzed samples); (b) DR ($\Delta TPV/V_O \times 100\%$) of total pores, macropores, mesopores and micropores.

(Fig. 12). What's more, the major peak pore size was less in Y11-SC-500 than in Y11–C-500 (Fig. 7c and d). All evidence indicated that OM pores in Y2 and Y11 at the dry gas stage from the semi-closed system were much smaller than pores from the closed system. It is speculated that the pressure exerted in the semi-closed system influenced the pore size. One possibility is that large pores were compacted into smaller ones during thermal simulation in the semi-closed system; another possibility is that, in the semi-closed system, pores were small when they were first generated during thermal simulation. In the semi-closed system, the OM skeleton is compacted by the vertical pressure before oil and gas generation. Otherwise, the OM is not compacted in the closed system. During thermal maturation, large amounts of gas and volatile fluids are generated. The fluid pressure is larger in the semi-closed system, and gas and other volatile fluids are easily compacted. Smaller gas bubbles with higher pressure could be present in the semi-closed system, when compared with the closed system (fluid pressure less than 300 kPa). In terms of MM15, as oil was the major product in both pyrolysis systems and liquid fluid was difficult to be compacted, the pressure in semi-closed system could barely influence the pore structure during OM transformation. However, once the liquid fluid was expelled, the overburden pressure in the semi-closed system might have compacted some of the pores generated, leading to smaller average pore diameter (Fig. 6d and e and Table 1).

### 4.2. Implications for porosity calculation of matured shale samples

The TOC content of the original sample (TOCo) and pyrolyzed shale samples were used to calculate the organic porosity (shale porosity increase due to organic matter expulsion) and kerogen porosity (the ratio between the generated pore volume as a result of OM expulsion and kerogen volume of the original shale sample) to illustrate the effect of OM compositions on the pore development of shale samples.

#### 4.2.1. Organic porosity calculation

The organic porosity (Φop) was estimated by converting the amount of transformed and expelled carbon (Cexpell) to the corresponding mass of kerogen and then calculating a reduced volume percentage occupied by kerogen (Chen and Jiang, 2016), which can be expressed in the following form.

$$\Phi op = [(\text{Cexpell} \times \gamma) / \text{kerogen density}] / [1 / \text{shale density}], \quad (1)$$

$$\Phi kp = [\text{Cexpell} \times 1.2/\text{kerogen density}]/[\text{TOCo} \times 1.2/\text{kerogen density}], \quad (2)$$

where Φop = organic porosity and Φkp = kerogen porosity; at different thermal maturities, the kerogen density and shale bulk density were assumed to be 1.2 g/cm$^3$ and 2.464 g/cm$^3$, respectively; by multiplying by the constant γ = 1.2, the total expelled OM masses were calculated from Cexpell.

The expelled organic carbon content is calculated by utilizing $TOC^X$, (the TOC content of the equivalent amount of original source rock after generation and expulsion of petroleum) introduced by Peters et al. (2005) in conjunction with the TOCo (Table 4).

$$\text{Cexpell} = \text{TOCo} - TOC^{X'}, \quad (3)$$

$$TOC^{X'} = TOC^X \times CF, \quad (4)$$

$$CF = (1000 - [S1^O + S2^O])/(1000 - [S1^X + S2^X]), \quad (5)$$

where $TOC^X$ is the measured TOC of the mature source rock; CF is the weight-loss correction factor (Peters et al., 2005); $S1^X$ and $S2^X$ are the measured S1 and S2 of the mature source rock; and $S1^O$ and $S2^O$ are the original S1 and S2 of the source rock.

In geological situations, the TOCo, $S1^O$, and $S2^O$ (HIo) of matured shale samples are unknown. As the original shale sample was immature, the $S1^O$ value is not significant to calculation precision. Different methods have been proposed to restore TOCo and HIo (Chen and Jiang, 2016; Han et al., 2017; Jarvie et al., 2007; Modica and Lapierre, 2012; Peters et al., 2005; Romero-Sarmiento et al., 2013). As the method presented by Modica and Lapierre (2012) does not consider expulsion efficiency, thus leading to an unrealistically high TOCo value, the methods of Chen and Jiang (2016) and Peters et al. (2005) were used to calculate the TOCo using data from pyrolyzed samples. A comparison of the calculated and measured TOCo values shows that the calculated value for the sample with TOCo of 5.28 wt% approximates the measured value (Fig. 15). However, for the two shale samples with types I and II OM and high TOC content, the calculated TOCo deviates considerably from the measured TOCo for Y2 in the closed system and MM15 in the semi-closed system (Fig. 15). The main reason for the discrepancy between the calculated and measured TOCo is that the assumed stable α (the ratio of convertible carbon to total carbon in the sample) defined in Chen and Jiang (2016) varies during the maturation processes, which is related to expulsion efficiency (Behar et al., 1997; Hill et al., 2003; Ungerer et al., 1988, Table 4). To precisely calculate Φop and Φkp, the measured TOCo and HIo were used.

Calculation results show that samples with type I OM have larger calculated organic porosity than samples with type II OM (Fig. 16a). The organic porosities of Y11 dominated by type III OM are notably lower than the other two samples. MM15 and Y2 have a much higher organic porosity in the semi-closed system than in the closed system (Fig. 16) and agree well with the much greater decrease in TOC content in the semi-closed system (Fig. 2). Y11 shows little difference in organic porosity for both pyrolysis systems (Fig. 16), consistent with similar TOC content variations (Figs. 2 and 13). The kerogen in MM15 with type I OM was more porous than Y2 and Y11 with type II and III OM, as well as for the semi-closed system than the closed system.

**Table 4**
Calculation of porosity based on the amount of expelled carbon.

| Sample | CF | $TOC^X$ | $TOC^{X'}$ | $Co^{X'}$ | $C_{L+R}^{X'}$ | $C_I^{X'}$ | Cexpell | kerogen porosity | organic porosity | α | Expulsion efficiency |
|---|---|---|---|---|---|---|---|---|---|---|---|
| | | (mg/g rock) | (mg/g rock) | (mg/g rock) | (mg/g rock) | (mg/g rock) | (mg/g rock) | (%) | (%) | (%) | (%) |
| MM15-O | | 175.2 | 175.2 | 1.3 | 100.2 | 73.6 | – | – | – | 57.99 | – |
| MM15-C-330 | 0.958 | 136.2 | 130.5 | 9.1 | 57.9 | 63.4 | 44.7 | 25.54 | 11.02 | 63.81 | 44.04 |
| MM15-C-350 | 0.937 | 126 | 118.1 | 15.2 | 35.1 | 67.8 | 57.1 | 32.58 | 14.05 | 61.30 | 56.26 |
| MM15-C-380 | 0.909 | 110.6 | 100.5 | 10.1 | 16.7 | 73.7 | 74.7 | 42.63 | 18.39 | 57.93 | 73.60 |
| MM15-C-420 | 0.882 | 96.5 | 85.1 | 2.6 | 1.8 | 80.6 | 90.1 | 51.45 | 22.19 | 54.00 | 88.77 |
| MM15-C-450 | 0.88 | 99.4 | 87.5 | 2.3 | 1 | 84.2 | 87.7 | 50.06 | 21.6 | 51.94 | 86.40 |
| MM15-C-500 | 0.879 | 111.1 | 97.7 | 2 | 0.5 | 95.2 | 77.5 | 44.25 | 19.09 | 45.66 | 76.35 |
| MM15-C-560 | 0.879 | 111.1 | 97.6 | 1.9 | 0.4 | 95.3 | 77.6 | 44.26 | 19.09 | 45.61 | 76.45 |
| MM15-O-SC | | 175.2 | 175.2 | 1.3 | 100.2 | 73.6 | – | – | – | 57.99 | – |
| MM15-SC-330 | 0.998 | 158.7 | 158.4 | 6.2 | 93.9 | 58.3 | 16.8 | 9.58 | 4.13 | 66.72 | 16.55 |
| MM15-SC-350 | 0.967 | 129.3 | 125 | 4.2 | 70 | 50.8 | 50.2 | 28.67 | 12.37 | 71.00 | 49.46 |
| MM15-SC-380 | 0.951 | 115.3 | 109.6 | 4.4 | 56.8 | 48.4 | 65.6 | 37.43 | 16.15 | 72.37 | 64.63 |
| MM15-SC-420 | 0.89 | 65.7 | 58.4 | 0.7 | 10.4 | 47.4 | 116.8 | 66.64 | 28.74 | 72.95 | 115.07 |
| MM15-SC-450 | 0.881 | 55.6 | 49 | 0.5 | 3.1 | 45.3 | 126.2 | 72.06 | 31.08 | 74.14 | 124.33 |
| MM15-SC-500 | 0.877 | 58.3 | 51.1 | 0 | 0.5 | 50.6 | 124.1 | 70.82 | 30.55 | 71.12 | 122.27 |
| MM15-SC-560 | 0.876 | 44.1 | 38.6 | 0 | 0.1 | 38.6 | 136.6 | 77.95 | 33.62 | 77.97 | 134.58 |
| Y11–O | | 52.8 | 52.8 | 3 | 9.3 | 40.6 | – | – | – | 23.11 | – |
| Y11–C-330 | 0.996 | 46.5 | 46.3 | 2.4 | 6.3 | 37.7 | 6.5 | 12.32 | 1.6 | 28.60 | 52.85 |
| Y11–C-350 | 0.992 | 46.5 | 46.1 | 1.9 | 3.5 | 40.7 | 6.7 | 12.67 | 1.65 | 22.92 | 54.47 |
| Y11–C-380 | 0.988 | 43.9 | 43.4 | 1.1 | 1.2 | 41.1 | 9.4 | 17.87 | 2.32 | 22.16 | 76.42 |
| Y11–C-420 | 0.987 | 44.7 | 44.1 | 0.6 | 0.7 | 42.8 | 8.7 | 16.47 | 2.14 | 18.94 | 70.73 |
| Y11–C-450 | 0.987 | 41.9 | 41.4 | 1.3 | 0.3 | 39.7 | 11.4 | 21.67 | 2.82 | 24.81 | 92.68 |
| Y11–C-500 | 0.987 | 41.3 | 40.7 | 1 | 0.2 | 39.6 | 12.1 | 22.83 | 2.97 | 25.00 | 98.37 |
| Y11–C-540 | 0.986 | 43.3 | 42.7 | 0.8 | 0.2 | 41.7 | 10.1 | 19.11 | 2.48 | 21.02 | 82.11 |
| Y11-SC-330 | 0.995 | 43.9 | 43.7 | 0.6 | 7.3 | 35.7 | 9.1 | 17.29 | 2.25 | 32.39 | 73.98 |
| Y11-SC-350 | 0.995 | 44.1 | 43.9 | 1.2 | 7.2 | 35.5 | 8.9 | 16.87 | 2.19 | 32.77 | 72.36 |
| Y11-SC-380 | 0.994 | 44 | 43.7 | 0.9 | 6.5 | 36.4 | 9.1 | 17.16 | 2.23 | 31.06 | 73.98 |
| Y11-SC-420 | 0.991 | 42.3 | 41.9 | 0.9 | 3.8 | 37.3 | 10.9 | 20.63 | 2.68 | 29.36 | 88.62 |
| Y11-SC-450 | 0.989 | 42.2 | 41.7 | 0.9 | 2.3 | 38.6 | 11.1 | 20.96 | 2.72 | 26.89 | 90.24 |
| Y11-SC-500 | 0.986 | 37.9 | 37.4 | 0 | 0.4 | 36.9 | 15.4 | 29.25 | 3.8 | 30.11 | 125.20 |
| Y11-SC-540 | 0.985 | 40.1 | 39.5 | 0 | 0.1 | 39.4 | 13.3 | 25.18 | 3.27 | 25.38 | 108.13 |
| Y2–O | | 186.9 | 186.9 | 2.7 | 65.6 | 118.6 | – | – | – | 36.54 | – |
| Y2–C-330 | 0.983 | 184.6 | 181.5 | 10 | 44.6 | 126.9 | 5.4 | 2.89 | 1.33 | 32.10 | 7.91 |
| Y2–C-350 | 0.973 | 182 | 177.1 | 15.8 | 30.3 | 131 | 9.8 | 5.27 | 2.42 | 29.91 | 14.35 |
| Y2–C-380 | 0.936 | 158.3 | 148.1 | 7.9 | 7.7 | 132.6 | 38.8 | 20.75 | 9.55 | 29.05 | 56.81 |
| Y2–C-420 | 0.923 | 160.9 | 148.5 | 2.8 | 2.5 | 143.2 | 38.4 | 20.52 | 9.44 | 23.38 | 56.22 |
| Y2–C-450 | 0.921 | 165.6 | 152.5 | 2.1 | 1.2 | 149.2 | 34.4 | 18.43 | 8.48 | 20.17 | 50.37 |
| Y2–C-500 | 0.919 | 163 | 149.7 | 1 | 0.5 | 148.2 | 37.2 | 19.89 | 9.15 | 20.71 | 54.47 |
| Y2–C-520 | 0.918 | 162.3 | 149.1 | 0.9 | 0.5 | 147.6 | 37.8 | 20.25 | 9.32 | 21.03 | 55.34 |
| Y2–C-540 | 0.919 | 157.5 | 144.7 | 0.9 | 0.6 | 143.1 | 42.2 | 22.59 | 10.39 | 23.43 | 61.79 |
| Y2–C-560 | 0.918 | 174 | 159.8 | 0.9 | 0.6 | 158.4 | 27.1 | 14.49 | 6.67 | 15.25 | 39.68 |
| Y2–C-600 | 0.917 | 173.5 | 159.2 | 0.3 | 0.2 | 158.6 | 27.7 | 14.84 | 6.83 | 15.14 | 40.56 |
| Y2-SC-330 | 1.008 | 202.9 | 204.6 | 1.7 | 73.4 | 129.4 | −17.7 | – | – | 30.77 | – |
| Y2-SC-350 | 1.002 | 203.3 | 203.7 | 6.7 | 63.1 | 133.8 | −16.8 | – | – | 28.41 | – |
| Y2-SC-380 | 0.96 | 177.8 | 170.7 | 6.2 | 29.4 | 135.1 | 16.2 | 8.67 | 3.99 | 27.72 | 23.72 |
| Y2-SC-420 | 0.931 | 160.7 | 149.6 | 5.6 | 6.1 | 137.9 | 37.3 | 19.96 | 9.18 | 26.22 | 54.61 |
| Y2-SC-450 | 0.919 | 134.6 | 123.7 | 0.1 | 1.7 | 121.9 | 63.2 | 33.83 | 15.56 | 34.78 | 92.53 |
| Y2-SC-500 | 0.917 | 127.2 | 116.7 | 0.1 | 0.5 | 116.1 | 70.2 | 37.57 | 17.29 | 37.88 | 102.78 |
| Y2-SC-520 | 0.918 | 134.1 | 123.1 | 0.2 | 0.9 | 122 | 63.8 | 34.13 | 15.71 | 34.72 | 93.41 |
| Y2-SC-540 | 0.917 | 135.2 | 124 | 0 | 0.5 | 123.5 | 62.9 | 33.64 | 15.48 | 33.92 | 92.09 |
| Y2-SC-560 | 0.917 | 130.6 | 119.7 | 0 | 0.1 | 119.6 | 67.2 | 35.94 | 16.54 | 36.01 | 98.39 |

Notes.

a. α is the ratio of convertible carbon to total carbon in the sample. In shale samples, the TOC is made up of convertible carbon and inert carbon. In the original shale, the convertible carbon content includes the carbon in S1 and S2, and the rest is inert carbon (Because of the small organic carbon content in S3, for convenience of calculation, it is regarded as inert carbon). For mature shale, the convertible carbon content is the carbon in expelled OM and residual S1 and S2, and the rest is inert carbon.

b. According to Eseme et al. (2012), $Co = S1 \times 0.82$; $C_{L+R} = S2 \times 0.82$; $C_I = TOC - Co - C_{L+R}$. Similar to the calculation of $TOC^{X'}$, $Co^{X'} = Co^X \times CF$; $C_{L+R}^{X'} = C_{L+R}^X \times CF$;

$C_I^{X'} = TOC^{X'} - Co^{X'} - C_{L+R}^{X'}$. Cexpell = TOCo − $TOC^{X'}$.
c. Expulsion efficiency = Cexpell/(TOCo – $C_I$ of the original samples).

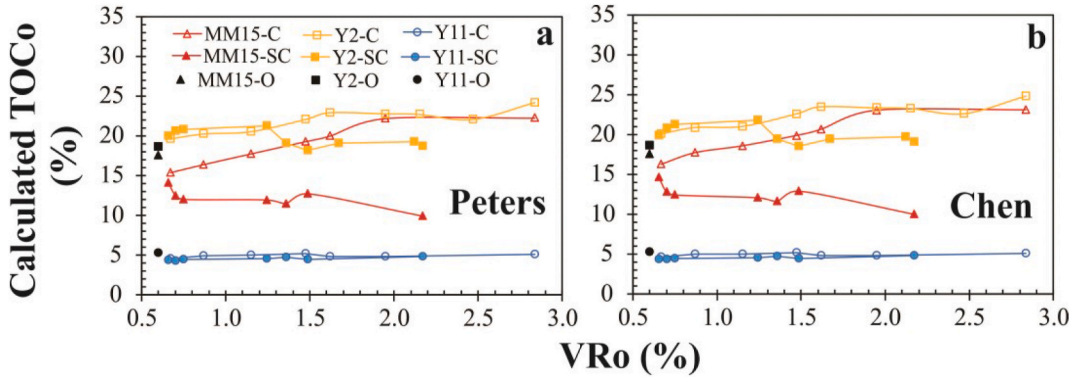


**Fig. 15.** Comparison between measured and calculated TOCo by using the methods of (a) Peters et al. (2005), and (b) Chen and Jiang (2016).

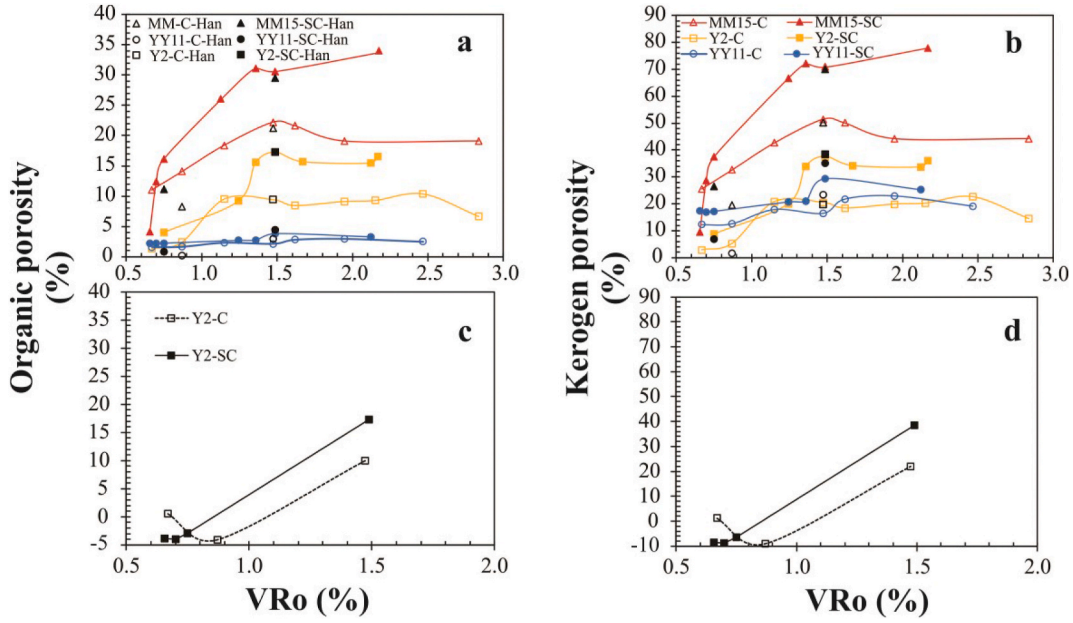


**Fig. 16.** (a) Organic porosity, and (b) kerogen porosity calculated using the proposed method and a kerogen density of 1.2 g/cm$^3$; (c) organic porosity, and (d) kerogen porosity calculated using the proposed method and kerogen density reported by Han et al. (2017). According to Han et al. (2017), the kerogen density of a shale sample with a VRo of 0.53% is 1.226 g/cm$^3$, then the density decreases to 1.096 g/cm$^3$ when the VRo increases to 0.85%. Afterwards the density increases to 1.355 g/cm$^3$ when the VRo is 1.45%. When calculating the organic porosity and kerogen porosity presented in panels c and d, the kerogen densities for the samples used is listed as followed: 1.226 g/cm$^3$ for VRo range of 0.50–0.67%, 1.096 g/cm$^3$ for VRo range of 0.75–0.87%, and 1.355 g/cm$^3$ for VRo range of 1.47–1.49%. Fig. 16a and b share legends.

During thermal maturation, kerogen density changes with the evolution of OM. According to Han et al. (2017), kerogen density decreases with increasing thermal maturity and then increases afterwards, and the lowest value occurs at the oil generation stage. This result differs from the classic assumption and measured result that the density of type II kerogen increases with increasing maturity (Ungerer et al., 1981; Okiongbo et al., 2005; Rudnicki, 2016). The density of organic matter in Han et al. (2017) was based on solvent unextracted kerogen, which may account for the discrepancy. By using the measured density of kerogens with different thermal maturities from the Posidonia Shale (Han et al., 2017), the organic porosity and kerogen porosity were calculated from Eqs. (1) and (2), and the results are presented in Fig. 16c and d. For pyrolyzed samples with Ro = 1.5%, the calculated values are comparable with the results using the proposed method (Fig. 16a and b). Similar to this work, other theoretical studies, assuming a constant kerogen density or an increasing kerogen density with thermal maturity, have shown that a great increase in organic porosity appears during the oil window (Modica and Lapierre, 2012; Romero-Sarmiento et al., 2013). However, if the decrease of kerogen density at the oil generation stage is considered (Han et al., 2017), organic porosity and kerogen porosity present their lowest values (Fig. 16c and d). The lowest measured pore volume in both pyrolyzed and geological shale is also observed at the oil window (Guo et al., 2014, 2017; Mastalerz et al., 2013; Valenza et al., 2013). This proves that, although there is OM expulsion and accordingly OM content decrease at the oil generation stage, the kerogen density decrease could still lead to porosity decrease.

#### 4.2.2. *Possible large influence of geological processes on shale porosity*

When calculating shale porosity, the organic porosity of shale samples may be compared with the overall porosity (Modica and Lapierre,

2012; Romero-Sarmiento et al., 2013), as it is assumed that mineral pores in the matrix are water-wet (Modica and Lapierre, 2012). Reports of the porosity of shales at different thermal maturity measured by helium pycnometry were collected and compared with the porosities of the pyrolyzed samples in this study (Guo et al., 2018; Han et al., 2017; Mastalerz et al., 2013; Milliken et al., 2013; Pan et al., 2015; Tian et al., 2013, 2015, Fig. 17). With the exception of Posidonia Shale of northern Germany, the porosity at different thermal maturities ranged between 1 and 10% (Fig. 17). Posidonia Shale with type II OM has never been deeply buried but was thermally matured by a deep-seated igneous intrusion (Han et al., 2017) and its porosity was not influenced by compaction to any great extent. As a result, the porosity of high-maturity Posidonia Shale (Ro = 1.45%) is 8%–16%, larger than in other shale plays.

The calculated porosities of pyrolyzed Y11 samples from both pyrolysis systems and of Y2 from the closed system lie within the range of actual geological shale porosities (Fig. 17). The porosity of Y2 from the semi-closed system is similar to some of the Posidonia Shale (Han et al., 2017, Fig. 17). Both Y2 and Posidonia Shale contain type II OM and high TOC content (18 wt% for Y2 and 10.41 wt% for low-maturity Posidonia Shale; Littke et al., 1988; Han et al., 2017). Y2 from the semi-closed system and Posidonia Shale (average TOC content of 6.75 wt% for samples with Ro = 1.45%) both show a decrease of about 4–5 wt% in TOC content. Accordingly, they have similar porosities at the high-maturity stage. It seems that high expulsion efficiency might exist in geological situations. The calculated porosity of MM15 (type I OM) differs considerably from the porosity of geological shale.

The high OM expulsion efficiency of pyrolyzed samples might be partially responsible for the higher shale porosity when compared with the geological shale samples. The expulsion efficiency of pyrolyzed samples was calculated and listed in Table 4. The high expulsion efficiency of pyrolyzed shale samples at the high-over-mature stage from the semi-closed system might not exist in the geological situations. The high expulsion efficiency derived from the experimental data may be accentuated by the short migration distances due to sample size and flow rates and higher experimental temperature compared to nature (Eseme et al., 2012). And shale samples with low expulsion efficiency exist in natural situations (Leythaeuser et al., 1988). Therefore, calculations based on the experimental studies should be used with caution when trying to extrapolate into geological situations.

However, previous studies by using the routine geochemical measurements of matured shale samples from different formations, have shown that the expulsion efficiency of oil-prone source rocks is 80–90% at the peak oil generation stage, and accumulated expulsion efficiency is about 50% at the oil window for source rocks with type III OM (Baur et al., 2011; Chen et al., 2014; Cooles et al., 1986; Leythaeuser et al., 1988). Expulsion efficiency of pyrolyzed samples from lowmature to late oil generation stage was compared with that of natural source rocks of comparable thermal maturity. Except for pyrolyzed samples of MM15 from the semi-closed system, the expulsion efficiency of pyrolyzed samples at the oil generation stage is comparable to or lower than that of the natural samples of similar thermal maturity.

Shale porosity was calculated based on the kerogen volume loss. The calculated porosity for pyrolyzed samples of MM15 from the mature to late mature stage is higher than that of natural source rocks (Fig. 17). If it is assumed that the expulsion efficiency of Y2 is about 90% at the late oil stage, the calculated porosity would be 15%, which exceeds the porosity of most natural source rock. What's more, the transformation of kerogen into oil and gas would lead to volume expansion. During the calculation of organic porosity (shale porosity), the OM mass loss and corresponding volume increase was based on the density of solid kerogen and the expansion of OM was not considered. The cracking of kerogen into gas and oil would lead to volume expansion, as the density of oil and gas is lower than that of kerogen. The calculated pore volume or porosity might be larger for shale samples with high expulsion efficiency if the expansion of OM were considered. To sum up, in some cases, the expulsion efficiency of pyrolyzed samples at the oil generation stage is similar to or lower than that of natural samples. Higher calculated shale porosity of pyrolyzed samples compared to the natural samples might also be related to other factors.

The lack of constraints involving cementation and compaction might also be responsible for the higher calculated porosity of pyrolyzed samples of highly abundant type I/II OM than in the geological shale samples. Cementation by minerals and compaction of mineral-associated pores may reduce pore volume from the low-to high-maturity stage (Han et al., 2017; Pommer and Milliken, 2015). Calculation of the organic porosity of Barnett Shale (Northeast Texas, USA) was based on the assumption that nanometer-scale kerogen pores are probably far too small to be affected by overburden stress (Modica and Lapierre, 2012; Romero-Sarmiento et al., 2013). However, the lower porosity of shale samples with high TOC content seems not to support this view (Milliken et al., 2013). The stiffness of mineral grains and organic macerals may help to preserve organic pores. FE-SEM observations have shown that OM pores are more likely to be preserved within small OM domains, probably because they tend to be sheltered by rigid grains from the effect of compaction (Guo et al., 2018; Löhr et al., 2015; Mathia

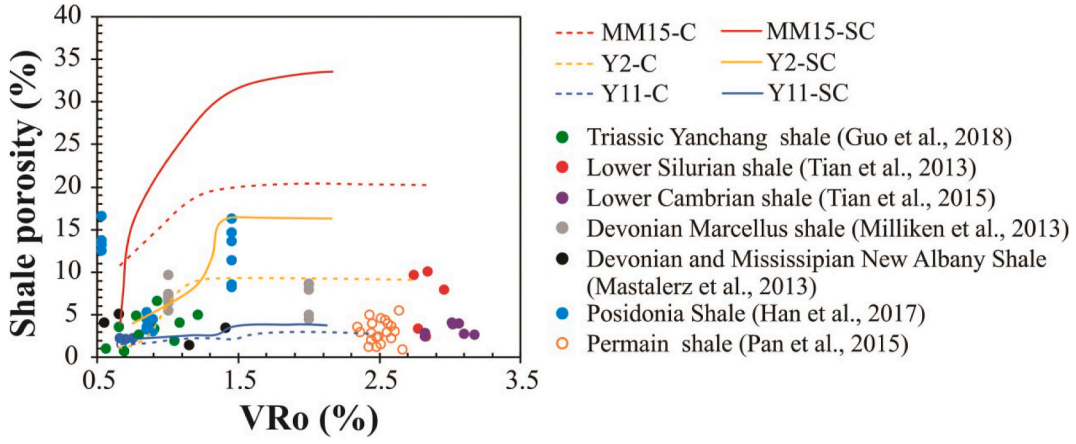


**Fig. 17.** Comparison between calculated porosity of pyrolyzed shale samples from this work and porosity of geological shale samples at different thermal maturities from published literatures. When calculating shale porosity, it is assumed that mineral pores in the matrix are water-wet (Modica and Lapierre, 2012). The organic porosity of shale samples may be comparable with the overall shale porosity (Modica and Lapierre, 2012; Romero-Sarmiento et al., 2013). The porosity of shales at different thermal maturities measured by helium pycnometry were collected (Han et al., 2017; Guo et al., 2018; Mastalerz et al., 2013; Milliken et al., 2013; Pan et al., 2015; Tian et al., 2013, 2015).

et al., 2016). For shale with high TOC content and type I/II OM, the cracking and expulsion of OM leads to the generation of micrometer-scale pores (Figs. 10 and 11; Fig. 21 in Ko et al., 2018, Fig. 10 in Liu et al., 2019). The micrometer-size pores in residual bitumen were observed in natural shale samples at the oil stage and it is interpreted as being associated with two-phase fluid inclusions (heavy oil/light oil, or oil/water, or oil/gas) (Guo et al., 2018; Loucks and Reed, 2014; Mathia et al., 2016). Under geological situations, these pores are generated during the migration or expulsion of oil, as liquid fluid cannot be compacted underground but is expelled when a large amount of oil is generated at the oil stage. Such large pores would not be preserved in situ at the high-over mature stage without the protection of rigid minerals such as carbonates (Mathia et al., 2016), as compaction would reduce the pore size. The high OM expulsion efficiency of pyrolyzed samples at the overmature stage, and the large amount of modifided mienral pores might not be prevalent in geological situations. Other meso- and macropores without the protection of rigid minerals might also be compacted. Moreover, the Posidonia Shale, New Albany Shale (Illinois Basin, USA) and Marcellus Shale (NE USA) have similar TOC range and type II OM (Han et al., 2017; Mastalerz et al., 2012; Obermajer et al., 1996). Uncompacted Posidonia Shale (Ro = 1.45%) clearly has a higher porosity than both New Albany Shale with similar thermal maturity and Marcellus Shale with higher thermal maturity, which further points to the reduction of pore volume by compaction. To precisely predict the porosity of shale by calculation, the effect of the above two factors on the limitation of pore volume needs further investigation.

## 5. Conclusions

Two shale samples (MM15 with type I kerogen and Y11with type III kerogen) were subjected to pyrolysis in two different systems and the pore development of pyrolyzed samples was characterized. By combining the results of these two samples with previously reported data for a sample (Y2) having type II kerogen (Guo et al., 2017), the effect of OM compositions on pore development during the artificially thermal maturing process was described. Some conclusions are drawn as follows.

(1) Pore volume evolution with thermal maturity, measured by gas adsorption, is closely related to the OM compositions. At the early oil generation stage, pore volume in shale samples with greater oil potential was more severely reduced by the residual bitumen, more so for micropores than meso- and macropores. Pore volume was observed to increase in two stages, possibly related mainly to the oil expulsion and to the release of larger amounts of light hydrocarbons and gases respectively. As a result, shales having types I/II kerogen show evident pore development in both two stages, while the shale containing type III kerogen mainly displays pore development in the later stage. Overall, in this study, shale having greater oil generation potential showed a greater extent of pore development in these stages. It should be noted that, since only three shale samples were investigated in this study, this conclusion should be used with caution.

(2) FE-SEM observation revealed subtle differences in the main pore types between these samples. For the sample with abundant type I kerogen, relatively large modified mineral pores were predominant in samples pyrolyzed by both methods, and were mainly associated with significant oil expulsion. By contrast, the pressurized semi-closed system produced more nanometer-sized OM pores than the closed system in the two samples having type II and type III kerogen. These spongy and complex OM resemble those developed in naturally matured samples, which have been associated with the expulsion or exsolution of gaseous hydrocarbons. Therefore, it seems that both the OM compositions and the pressure condition affect the pore types developed during pyrolysis.

(3) The organic porosity was calculated using the measured TOC content of original samples and TOC content corrected by the weight-loss correction factor for pyrolyzed samples. This revealed that the OM-rich shale sample that is more oil generative exhibits larger organic porosity increase with thermal maturation. The semi-closed pyrolysis system (which has a higher hydrocarbon expulsion efficiency) showed a greater porosity increase than the closed system. The difference in porosity between the two pyrolysis systems is larger for the shale sample with type I kerogen, when compared with the shale samples with type II and type III kerogen. These results are consistent with the results obtained by gas adsorption analysis.

(4) The calculated organic porosity of the OM-rich oil generative shale sample is larger than the measured porosity of geological shale samples. This might be related to the high expulsion efficiency of artificially matured samples. In addition, the lack of the constraints imposed by cementation and compaction might also be responsible for this. Besides the significant role of compaction in reducing the volume of pores associated with minerals at the early-mature to mature stage, it might also reduce the volume of pores associated with OM during oil cracking and expulsion.

## CRediT authorship contribution statement

**Huijuan Guo:** Investigation, Methodology, Writing - original draft. **Wanglu Jia:** Conceptualization, Funding acquisition, Writing - review & editing. **Ruliang He:** Investigation, Methodology. **Chiling Yu:** Resources, Data curation. **Jianzhong Song:** Visualization, Formal analysis. **Ping'an Peng:** Supervision, Funding acquisition, Writing - review & editing.

## Declaration of competing interest

The authors declare that they have no known competing financial interests or personal relationships that could have appeared to influence the work reported in this paper.

## Acknowledgements

This work was supported by the Strategic Priority Research Program (XDB10010204), National Oil and Gas Major Project (2017ZX05008-002-010), Natural Science Foundation of China (grant numbers 41803043 and 41621062), and the "135" Project of GIG-CAS (135TP201602). The authors thank Prof. Jialan Lu and Dr Jian Zeng for their assistance in the pyrolysis experiments, Dr Qin Zhou for the technical assistance in the FE-SEM observation and Dr Ming Cheng and Yuhong Lei for sample collection. Thanks to the editor Zhiye Gao and two reviewers for constructive comments that helped improve the quality of the manuscript.

## Appendix A. Supplementary data

Supplementary data to this article can be found online at https://doi.org/10.1016/j.marpetgeo.2020.104622.

## References

Ardakani, O.H., Sanei, H., Ghanizadeh, A., Lavoie, D., Chen, Z.H., Clarkson, C.R., 2017. Do all fractions of organic matter contribute equally in shale porosity? A case study from Upper Ordovician Utica Shale, southern Quebec, Canada. Mar. Petrol. Geol. 92, 794–808.

Alcantar-Lopez, L., 2016. Understanding organic matter structural changes with increasing thermal maturity from oil shale plays through SEM imaging. In: unconventional Resources Technology Conference, URTeC control ID number 2456170.

Barrett, E.P., Joyner, L.G., Halenda, P.P., 1951. The determination of pore volume and area distributions in porous substances. I. Computations from nitrogen isotherms. J. Am. Chem. Soc. 73, 373–380.

Baur, F., Primio, R.D., Lampe, C., Littke, R., 2011. Mass balance calculations for different models of hydrocarbon migration in the Jeanne D' arc basin, offshore Newfoundland. J. Petrol. Geol. 34, 181–198.
Behar, F., Vandenbroucke, M., Tang, Y., Marquis, F., Espitalie, J., 1997. Thermal cracking of kerogen in open and closed systems: determination of kinetic parameters and stoichiometric coefficients for oil and gas generation. Org. Geochem. 26, 321–339.
Bernard, S., Horsfield, B., Schulz, H.-M., Wirth, R., Schreiber, A., Sherwood, N., 2012. Geochemical evolution of organic-rich shales with increasing maturity: a STXM and TEM study of the Posidonia Shale (Lower Toarcian, northern Germany). Mar. Petrol. Geol. 31, 70–89.
Bustin, R.M., Bustin, A.M.M., Cui, A., Ross, D., Pathi, V.M., 2008. Impact of shale properties on pore structure and storage characteristics. In: SPE Shale Gas Production Conference. Society of Petroleum Engineers.
Cardott, B.J., Landis, C.R., Curtis, M.E., 2015. Post-oil solid bitumen network in the Woodford Shale, USA—a potential primary migration pathway. Int. J. Coal Geol. 139, 106–113.
Cardott, B.J., Curtis, M.E., 2018. Identification and nanoporosity of macerals in coal by scanning electron microscopy. Int. J. Coal Geol. 190, 205–217.
Carr, A.D., 2003. Thermal history model for the South Central Graben, North Sea, derived using both tectonics and maturation. Int. J. Coal Geol. 54, 3–19.
Cavelan, A., Boussafir, M., Le Milbeau, C., Rozenbaum, O., Laggoun-Défarge, F., 2019. Effect of organic matter composition on source rock porosity during confined anhydrous thermal maturation: example of Kimmeridge-clay mudstones. Int. J. Coal Geol. 212, 103236.
Chalmers, G.R., Bustin, R.M., 2008. Lower Cretaceous gas shales in northeastern British Columbia, Part I: geological controls on methane sorption capacity. Bull. Can. Petrol. Geol. 56, 1–21.
Chen, J., Xiao, X., 2014. Evolution of nanoporosity in organic-rich shales during thermal maturation. Fuel 129, 173–181.
Chen, J.P., Sun, Y.G., Zhong, N.N., Huang, Z.K., Deng, C.P., Xie, L.J., Han, H., 2014. The efficiency and model of petroleum expulsion from the lacustrine source rocks within geological frame. Acta Geol. Sin. 88, 2005–2032.
Chen, Z.H., Jiang, C.Q., 2016. A revised method for organic porosity estimation in shale reservoirs using Rock-Eval data: example from Duvernay Formation in the Western Canada Sedimentary Basin. AAPG (Am. Assoc. Pet. Geol.) Bull. 100, 405–422.
Chukwuma, K., Bordy, E.M., Coetzer, A., 2018. Evolution of porosity and pore geometry in the Permian Whitehill Formation of South Africa–A FE-SEM image analysis study. Mar. Petrol. Geol. 91, 262–278.
Cooles, G.P., Mackenzie, A.S., Quigley, T.M., 1986. Calculation of petroleum masses generated and expelled from source rocks. Adv. Org. Geochem. 10, 235–245.
CPSC (China Petroleum Standardization Committee, 2010. Analysis Method for Clay Minerals and Ordinary Non-clay Minerals in Sedimentary Rocks by X-ray Diffraction. SY/T 5163e2010.
Cui, J.W., Zhu, R.K., Cui, J.G., 2013. Relationship of porous evolution and residual hydrocarbon: evidence from modeling experiment with geological constains. Acta Geol. Sin. 87, 730–736.
Curtis, M.E., Ambrose, R.J., Sondergeld, C.H., Rai, C.S., 2011. Investigation of the relationship between organic porosity and thermal maturity in the Marcellus Shale. In: North American Unconventional Gas Conference and Exhibition. Society of Petroleum Engineers.
Dewhurst, D.N., Yang, Y., Aplin, A.C., 1999. Permeability and Fluid Flow in Natural Mudstones. Geological Society, vol. 158. Special Publications, London, pp. 23–43.
Dong, T., Harris, N.B., Ayranci, K., Twemlow, C.E., Nassichuk, B.R., 2017. The impact of composition on pore throat size and permeability in high maturity shales: middle and Upper Devonian Horn River Group, northeastern British Columbia, Canada. Mar. Petrol. Geol. 81, 220–236.
Eseme, E., Krooss, B.M., Littke, R., 2012. Evolution of petrophysical properties of oil shales during high-temperature compaction tests: Implications for petroleum expulsion. Mar. Petrol. Geol. 31, 110–124.
Fishman, N.S., Hackley, P.C., Lowers, H.A., Hill, R.J., Egenhoff, S.O., Eberl, D.D., Blum, A.E., 2012. The nature of porosity in organic-rich mudstones of the upper jurassic kimmeridge clay formation, north sea, offshore United Kingdom. Int. J. Coal Geol. 103, 32–50.
Furmann, A., Mastalerz, M., Schimmelmann, A., Pedersen, P.K., Bish, D., 2014. Relationships between porosity, organic matter, and mineral matter in mature organic-rich marine mudstones of the Belle Fourche and Second White Specks formations in Alberta, Canada. Mar. Petrol. Geol. 54, 65–81.
Groen, J.C., Peffer, L.A.A., Perez-Ramırez, J., 2003. Pore size determination in modified micro- and mesoporous materials. Pitfalls and limitations in gas adsorption data analysis. Microporous Mesoporous Mater. 60, 1–17.
Guo, H., Wang, X., Zhang, L., Jiang, C., Jia, W., Peng, P.a., Lei, Y., Luo, X., Cheng, M., 2014. Adsorption of $N_2$ and $CO_2$ on mature shales before and after extraction and its implication for investigations of pore structures. Geochimica 43, 408–414 (in Chinese with English abstract).
Guo, H.J., Jia, W.L., Peng, P.A., Zeng, J., He, R.L., 2017. Evolution of organic matter and nanometer-scale pores in an artificially matured shale undergoing two distinct types of pyrolysis: a study of the Yanchang Shale with Type II kerogen. Org. Geochem. 105, 56–66.
Guo, H., He, R., Jia, W., Peng, P.a., Lei, Y., Luo, X., Wang, X., Zhang, L., Jiang, C., 2018. Pore characteristics of lacustrine shale within the oil window in the upper triassic Yanchang Formation, southeastern Ordos Basin, China. Mar. Petrol. Geol. 91, 279–296.
Guo, M., Zhou, W., Li, R., Yu, D., 2009. Analysis on oil shale forming conditions in Maoming Basin of guangdong province. Geology and Mineral Resources of South China 2, 47–51 (in Chinese with English abstract).
Han, Y., Horsfield, B., Wirth, R., Mahlstedt, N., Bernard, S., 2017. Oil retention and porosity evolution in organic rich shales. AAPG (Am. Assoc. Pet. Geol.) Bull. 101, 807–827.
Hao, F., Zou, H.Y., Gong, Z.S., Yang, S.G., Zeng, Z.P., 2007. Hierarchies of overpressure retardation of organic matter maturation: cse studies from petroleum basins in China. AAPG (Am. Assoc. Pet. Geol.) Bull. 91, 1467–1498.
Hill, R.J., Tang, Y., Kaplan, I.R., 2003. Insights into oil cracking based on laboratory experiments. Org. Geochem. 34, 1651–1672.
Hu, H.Y., Zhang, T.W., Wiggins-Camacho, J.D., Ellis, G.S., Lewan, M.D., Zhang, X.L., 2015. Experimental investigation of changes in methane adsorption of bitumen-free Woodford Shale with thermal maturation induced by hydrous pyrolysis. Mar. Petrol. Geol. 59, 114–128.
Hunt, J.M., 1991. Generation of gas and oil from coal and other terrestrial organic matter. Org. Geochem. 17, 673–680.
Jarvie, D.M., Hill, R.J., Ruble, T.E., Pollastro, R.M., 2007. Unconventional shale-gas systems: the Mississippian Barnett Shale of north-central Texas as one model for thermogenic shale-gas assessment. AAPG (Am. Assoc. Pet. Geol.) Bull. 91, 475–499.
Ji, L.M., Su, L., Wu, Y.D., He, C., 2017. Pore evolution in hydrocarbon-generation simulation of organic matter-rich muddy shale. Petroleum Research 2, 146–155.
Katz, B.J., Arango, I., 2018. Organic porosity: a geochemist's view of the current state of understanding. Org. Geochem. 123, 1–16.
Kelemen, S., Walters, C., Ertas, D., Kwiatek, L., Curry, D., 2006. Petroleum expulsion Part 2. Organic matter type and maturity effects on kerogen swelling by solvents and thermodynamic parameters for kerogen from regular solution theory. Energy Fuel. 20, 301–308.
Klaver, J., Desbois, G., Urai, J.L., Littke, R., 2015. BIB-SEM characterization of the pore space morphology and distribution in postmature to overmature samples from the Haynesville and Bossier Shales. Mar. Petrol. Geol. 59, 451–466.
Ko, L.T., Loucks, R.G., Zhang, T.W., Rupple, S.C., Shao, D.Y., 2016. Pore and pore network evolution of Upper Cretaceous Boquillas (Eagle Ford-equivalent) mudrocks: results from gold tube pyrolysis experiments. AAPG (Am. Assoc. Pet. Geol.) Bull. 100, 1693–1722.
Ko, L.T., Loucks, R.G., Milliken, K.L., Liang, Q., Zhang, T., Sun, X., Hackley, P.C., Ruppel, S.C., Peng, S., 2017. Controls on pore types and pore-size distribution in the Upper Triassic Yanchang Formation, Ordos Basin, China: Implications for pore-evolution models of lacustrine mudrocks. Interpretation 5, SF127–SF148.
Ko, L.T., Ruppel, S.C., Loucks, R.G., Hackley, P.C., Zhang, T., Shao, D., 2018. Pore-types and pore-network evolution in Upper Devonian-Lower Mississippian Woodford and Mississippian Barnett mudstones: insights from laboratory thermal maturation and organic petrology. Int. J. Coal Geol. 190, 3–28.
Kuila, U., Prasad, M., 2013. Specific surface area and pore-size distribution in clays and shales. Geophys. Prospect. 61, 341–362.
Löhr, S.C., Baruch, E.T., Hall, P.A., Kennedy, M.J., 2015. Is organic pore development in gas shales influenced by the primary porosity and structure of thermally immature organic matter? Org. Geochem. 87, 119–132.
Lei, Y., Luo, X., Wang, X., Zhang, L., Jiang, C., Yang, W., Yu, Y., Cheng, M., Zhang, L., 2015. Characteristics of silty laminae in Zhangjiatan Shale of southeastern Ordos Basin, China: Implications for shale gas formation. AAPG (Am. Assoc. Pet. Geol.) Bull. 99, 661–687.
Leythaeuser, D., Schaefer, R.G., Radke, M., 1988. Geocheical effects of primary migration of petroleum in Kimmeridge source rocks from Brae field area, North Sea. I: gross composition of $C_{15+}$ -soluble organic matter and molecular composition of $C_{15+}$-satuated hydrocarbons. Geochem. Cosmochim. Acta 52, 701–713.
Li, J., Zhou, S.X., Li, Y.J., Ma, Y., Yang, Y.A., Li, C.C., 2016. Effect of organic matter on pore structure of mature lacustrine organic-rich shale: a case study of the Triassic Yanchang shale, Ordos Basin, China. Fuel 185, 421–431.
Littke, R., Barker, D.R., Leythaeuser, D., 1988. Microscopic and sedimentologic evidence for the generation and migration of hydrocarbons in Toarcian source rocks of different maturities. Org. Geochem. 13, 549–559.
Liu, B., Schieber, J., Mastalerz, M., 2017a. Combined SEM and reflected light petrography of organic matter in the New Albany Shale (Devonian-Mississippian) in the Illinois Basin: a perspective on organic pore development with thermal maturation. Int. J. Coal Geol. 184, 57–72.
Liu, Y.K., Xiong, Y.Q., Li, Y., Peng, P.A., 2017b. Effects of oil expulsion and pressure on nanopore development in highly mature shale: evidence from a pyrolysis study of the Eocene Maoming oil shale, south China. Mar. Petrol. Geol. 86, 526–536.
Liu, D.Y., Li, H.C., Zhang, C., Wang, Q.T., Peng, P.A., 2019. Experimental investigation of pore development of the Chang 7 member shale in the Ordos basin under semi-closed high-pressure pyrolysis. Mar. Petrol. Geol. 99, 17–26.
Liu, K.Q., Ostadhassan, M., Zhou, J., Gentzis, T., Rezaee, R., 2017c. Nanoscale pore structure characterization of the Bakken shale in the USA. Fuel 209, 567–578.
Loucks, R.G., Ruppel, S.C., Wang, X., Ko, L., Peng, S., Zhang, T., Rowe, H.D., Smith, P., 2017. Pore types, pore-network analysis, and pore quantification of the lacustrine shale-hydrocarbon system in the Late Triassic Yanchang Formation in the southeastern Ordos Basin, China. Interpretation 5, SF63–SF79.
Loucks, R.G., Reed, R.M., 2014. Scanning-electron-microscope petrographic evidence for distinguishing organic-matter pores associated with depositional organic matter versus migrated organic matter in mudrock. Gulf Coast Association of Geological Societies 3, 51–60.
Loucks, R.G., Reed, R.M., Ruppel, S.C., Hammes, U., 2012. Spectrum of pore types and networks in mudrocks and a descriptive classification for matrix-related mudrock pores. AAPG (Am. Assoc. Pet. Geol.) Bull. 96, 1071–1098.
Loucks, R.G., Reed, R.M., Ruppel, S.C., Jarvie, D.M., 2009. Morphology, genesis, and distribution of nanometer-scale pores in siliceous mudstones of the mississippian Barnett shale. J. Sediment. Res. 79, 848–861.

Lu, J.M., Ruppel, S.C., Bowe, H.D., 2015. Organic matter pores and oil generation in the Tuscaloosa marine shale. AAPG (Am. Assoc. Pet. Geol.) Bull. 99, 333–357.
Mastalerz, M., Schimmelmann, A., Drobniak, A., Chen, Y., 2012. Influence of maceral composition on geochemical characteristics of immature shale kerogen: insights from density fraction analysis. Int. J. Coal Geol. 103, 60–69.
Mastalerz, M., Schimmelmann, A., Drobniak, A., Chen, Y., 2013. Porosity of Devonian and Mississippian New Albany Shale across a maturation gradient: insights from organic petrology, gas adsorption, and mercury intrusion. AAPG (Am. Assoc. Pet. Geol.) Bull. 97, 1621–1643.
Mastalerz, M., Wei, L., Drobniak, A., Schimmelmann, A., Schieber, J., 2018. Responses of specific surface area and micro-and mesopore characteristics of shale and coal to heating at elevated hydrostatic and lithostatic pressures. Int. J. Coal Geol. 197, 20–30.
Mathia, E.J., Bowen, L., Thomas, K.M., Aplin, A.C., 2016. Evolution of porosity and pore types in organic-rich, calcareous, Lower Toarcian Posidonia Shale. Mar. Petrol. Geol. 75, 117–139.
Milliken, K.L., Rudnicki, M., Awwiller, D.N., Zhang, T., 2013. Organic matter-hosted pore system, Marcellus formation (devonian), Pennsylvania. AAPG (Am. Assoc. Pet. Geol.) Bull. 97, 177–200.
Modica, C.J., Lapierre, S.G., 2012. Estimation of kerogen porosity in source rocks as a function of thermal transformation: example from the Mowry Shale in the Powder River Basin of Wyoming. AAPG Bull. 96, 87–108.
Noyan, H., Önal, M., Sarikaya, Y., 2006. The effect of heating on the surface area, porosity and surface acidity of a bentonite. Clay Clay Miner. 54, 375–381.
Obermajer, M., Fowler, M.G., Goodarzi, F., Snowdon, L.R., 1996. Assessing thermal maturity of Palaeozoic rocks from reflectance of chitinozoa as constrained by geochemical indicators: an example from southern Ontario, Canada. Marine and Peroleum Geology 13, 907–919.
Okiongbo, K.S., Aplin, A.C., Larter, S.R., 2005. Changes in type II keorgen density as a function of maturity: evience from the Kimmeridge clay formation. Energy Fuel. 19, 2495–2499.
Pan, L., Xiao, X., Tian, H., Zhou, Q., Chen, J., Li, T., Wei, Q., 2015. A preliminary study on the characterization and controlling factors of porosity and pore structure of the Permian shales in Lower Yangtze region, Eastern China. Int. J. Coal Geol. 146, 68–78.
Pepper, A.S., Corvi, P.J., 1995. Simple kinetic-models of petroleum formation. Part III. Modelling an open system. Mar. Petrol. Geol. 12, 417–452.
Peters, K.E., Walters, C.C., Moldowan, J.M., 2005. In: The Biomarker Guide. Biomarkers & Isotopes in Petroleum Systems & Earth History, vol. 2, p. 490.
Peters, K.E., Hackley, P.C., Thomas, J.J., Pomerantz, A.E., 2018. Suppression of vitrinite reflectance by bitumen generated from liptinite during hydrous pyrolysis of artificial source rock. Org. Geochem. 125, 220–228.
Pommer, M., Milliken, K., 2015. Pore types and pore-size distributions across thermal maturity, Eagle Ford Formation, southern Texas. AAPG (Am. Assoc. Pet. Geol.) Bull. 99, 1713–1744.
Romero-Sarmiento, M., Ducros, M., Carpentier, B., Lorant, F., Cacas, M., Pegaz-Fiornet, S., Wolf, S., Rohais, S., Moretti, I., 2013. Quantitative evaluation of TOC, organic porosity and gas retention distribution in a gas shale play using petroleum system modeling: application to the Mississippian Barnett Shale. Mar. Petrol. Geol. 45, 315–330.
Ross, D.J.K., Bustin, M.R., 2009. The importance of shale composition and pore structure upon gas storage potential of shale gas reservoirs. Mar. Petrol. Geol. 26, 916–927.
Rudnicki, M.D., 2016. Variation of organic matter density with thermal maturity. AAPG (Am. Assoc. Pet. Geol.) Bull. 100, 17–22.
Seewald, J.S., Eglinton, L.B., Ong, Y.L., 2000. An experimental study of organic-inorganic interactions during vitrinite maturation. Geochimica et Cosmochinica Acta 64, 1577–1591.
Sing, K.S., 1985. Reporting physisorption data for gas/solid systems with special reference to the determination of surface area and porosity (Recommendations 1984). Pure Appl. Chem. 57, 603–619.
Sun, L.N., Tuo, J.C., Zhang, M.F., Wu, C.J., Wang, Z.X., Zheng, Y.W., 2015. Formation and development of the pore structure in Chang 7 member oil-shale from Ordos Basin during organic matter evolution induced by hydrous pyrolysis. Fuel 158, 549–557.
Tian, H., Pan, L., Xiao, X.M., Wilkins, R.W.T., Meng, Z.P., Huang, B.J., 2013. A preliminary study on the pore characterization of Lower Silurian black shales in the Chuandong Trust Fold Belt, southwestern China using low pressure $N_2$ adsorption and FE-SEM methods. Mar. Petrol. Geol. 48, 8–19.
Tian, H., Pan, L., Zhang, T., Xiao, X., Meng, Z., Huang, B., 2015. Pore characterization of organic-rich lower Cambrian shales in Qiannan depression of Guizhou province, Southwestern China. Mar. Petrol. Geol. 62, 28–43.
Ungerer, P., Behar, F., Discamps, D., 1981. Tentative calculation of the overall volume expansion of organic matter during hydrocarbon genesis from geochemistry data. Implications for primary migration. Adv. Org. Geochem. 10, 129–135.
Ungerer, P., Behar, F., Villalba, M., Heum, O.R., 1988. Kinetic modeling of oil cracking. Adv. Org. Geochem. 13, 857–868.
Valenza, J.J., Drenzek, N., Marques, F., Pagels, M., Mastalerz, M., 2013. Geochemical controls on shale microstructure. Geology 41, 611–614.
Wang, X.Z., Gao, S.L., Gao, C., 2014. Geological features of Mesozoic continental shale gas in south of Ordos Basin, NW China. Petroelum exploration and development 41, 294–304.
Wang, Y., Liu, L.F., Hu, Q.H., Hao, L.W., Wang, X.M., Sheng, Y., 2019. Nanoscale pore network evolution of Xiamaling marine shale during organic matter maturation by hydrous pyrolysis. Energy Fuel. 34, 1548–1563.
Wei, L., Mastalerz, M., Schimmelmann, A., Chen, Y., 2014. Influence of Soxhlet-extractable bitumen and oil on porosity in thermally maturing organic-rich shales. Int. J. Coal Geol. 132, 38–50.
Wu, S.T., Zhu, R.K., Cui, J.G., Cui, J.W., Bai, B., Zhang, X.X., Jin, X., Zhu, D.S., You, J.C., Li, X.H., 2015. Characteristics of lacustrine shale porosity evolution, triassic Chang 7 member, Ordos Basin, NW China. Petrol. Explor. Dev. 42, 167–176.
Yang, H., Li, S.X., Liu, X.Y., 2013. Characteristics and resource prospects of tight oil and shale oil in Ordos Basin. Acta Pet. Sin 34, 1–11 in Chinese with English abstract.
Yang, S.Y., Schulz, H.M., Horsfield, B., Schovsbo, N.H., Noah, M., Panova, E., Rothe, H., Hahne, K., 2018. On the changing petroleum generation properties of Alum Shale over geological time caused by uranium irradiation. Geochem. Cosmochim. Acta 229, 20–35.
Zargari, S., Canter, K.L., Prasad, M., 2015. Porosity evolution in oil-prone source rocks. Fuel 153, 110–117.
Zeng, J., Jia, W., Peng, P.a, Guan, C., Zhou, C., Yuan, X., Chen, S., Yu, C., 2016. Composition and pore characteristics of black shales from the ediacaran lantian Formation in the yangtze block, south China. Mar. Petrol. Geol. 76, 246–261.
Zou, C.N., Zhu, R.K., Chen, Z.Q., Ogg, J.G., Wu, S.T., Dong, D.Z., Qiu, Z., Wang, Y.M., Wang, L., Lin, S.H., Cui, J.W., Su, L., Yang, Z., 2019. Organic-matter-rich shales of China. Earth Sci. Rev. 189, 51–78.